

BUILDING PRACTICAL APERTURELESS SCANNING NEAR-FIELD MICROSCOPY

by

M. ZEKI GUNGORDU

SEONGSIN MARGARET KIM, COMMITTEE CHAIR
PATRICK KUNG
ABIDIN YILDIRIM

A THESIS

Submitted in partial fulfillment of the requirements
for the degree of Master of Science
in the Department of Electrical and Computer Engineering
in the Graduate School of
The University of Alabama

TUSCALOOSA, ALABAMA

2017

ABSTRACT

The fundamental objective of this study is to establish a functional, practical apertureless type scanning near-field optical microscope, and to figure out the working mechanism behind it. Whereas a far-field microscope can measure the propagating field's components, this gives us little information about the features of the sample. The resolution is limited to about half of the wavelength of the illuminating light. On the other hand, the a-SNOM system enables achieving non-propagating components of the field, which provides more details about the sample's features. It is really difficult to measure because the amplitude of this field decays exponentially when the tip is moved away from the sample. The sharpness of the tip is the only limitation for resolution of the a-SNOM system. Consequently, the sharp tips are achieved by using electrochemical etching, and these tips are used to detect near-field signal. Separating the weak a-SNOM system signals from the undesired background signal, the higher demodulation background suppression is utilized by lock-in detection.

DEDICATION

This thesis is dedicated to my dear wife Nahide.

LIST OF ABBREVIATIONS AND SYMBOLS

nm	Nanometer
um	Micrometer
SEM	Scanning Electron Microscopy
STM	Scanning Tunneling Microscopy
AFM	Atomic Force Microscopy
TEM	Transmission Electron Microscopy
a-SNOM	Apertureless-Type Scanning Near Field Optical Microscope
s-SNOM	Scattering-Type Scanning Near Field Optical Microscope
SPM	Scanning Probe Microscopy
NF	Near-field
FF	Far-field
PSTM	Photon Scanning Tunneling Microscopy
STOM	Scanning Tunneling Optical Microscopy
SNR	Signal-to-noise ratio
PMT	Photomultiplier Tube
PCC	Parasitic Capacitance Compensation
MoS ₂	Molybdenum disulfide
TMDCs	Transition Metal Dichalcogenides
LTMD	Layered Transition Metal Dichalcogenide
PL	Photoluminescence

THz	Terahertz
TDS	Time Domain Spectroscopy
BS	Beam Splitter
PCA	Photoconductive Antenna
PE	Polyethylene

ACKNOWLEDGEMENTS

This thesis could not be accomplished without the help from many important people. I would like to thank my advisor, Dr. Seongsin Margaret Kim, for providing me with many outstanding opportunities to begin to form my character as a researcher. The skill and experience I have gained under her guidance have prepared me very well for my future.

I also would like to thank my committee members, Dr. Patrick Kung and Dr. Abidin Yildirim, for their time and willingness to serve on my thesis committee, support my work, and provide worthy comments to add value to my thesis.

In addition, I would like to thank all of my past and current fellow colleagues who accompanied me and helped me with any obstacle during the research and real life throughout my study.

Finally, I would like to thank my wife Nahide for her endless support and confidence in me. Without her dedication and constant love, this study would have not materialized.

CONTENTS

ABSTRACT.....	ii
DEDICATION.....	iii
LIST OF ABBREVIATIONS AND SYMBOLS	iv
ACKNOWLEDGEMENTS.....	vi
LIST OF FIGURES	x
CHAPTER 1 INTRODUCTION	1
1.1 Diffraction Limit.....	2
1.2 Scanning Probe Microscopy	6
1.3 The Development of SNOM.....	9
CHAPTER 2 A-SNOM THEORY AND MEASUREMENT TECHNIQUES	12
2.1 Confinement and Enhancement of Field.....	12
2.1.1 Lightning Rod Effect	14
2.1.2 Optical Antenna Effect.	16
2.1.3 Localized Surface Plasmon Resonance.	16
2.2 Theoretical Models for Tip Sample Interaction.....	17
2.2.1 Tip Spheroid Model	18
2.2.2 Point Dipole Model.....	20
2.2.3 Monopole Model.....	22

2.3 Near Field Signal Detection Techniques	24
2.3.1 Self-Homodyne Detection	26
2.3.2 Homodyne Detection	27
2.3.3 Pseudo-Heterodyne Detection	30
2.4 Background Suppression with Using Higher-Harmonic Demodulation	32
CHAPTER 3 EXPERIMENTAL SETUP	34
3.1 The SR830 Lock-in Amplifier	34
3.1.1 Software Development for Collecting Data from Lock-in Amplifier Remotely	34
3.1.1.1 VISA Communication VI	34
3.1.1.2 SubVIs for Specific Tasks	36
3.1.1.3 Main VI to Allows the User to Remotely Control the SR830 Lock-in Amplifier	38
3.2 Parabolic Mirror	40
3.3 Laser Source	41
3.4 Photomultiplier Tube (PMT)	41
3.5 Nanopositioning System via MadPLL Controller	42
3.6 Optical Alignment	48
CHAPTER 4 RESULTS	49
4.1 Preparing the Near-Field Tip by Electrochemical Etching Result	50
4.2 Near-Field Generation and Detection with Using Two Different Tungsten Tip	53
4.3 Near-Field Signal Excited Photoluminescence of MoS ₂ Result	61
CHAPTER 5 FUTURE WORK AND CONCLUSION	63
5.1 THz-Time Domain Spectroscopy (THz-TDS)	63

5.2 Integration of Near-Field System on THz-TDS.....	65
5.3 Conclusion	67
REFERENCES	68

LIST OF FIGURES

Figure 1.1 Light diffraction from a grating [15]	4
Figure 1.2 Scanning Probe Geometry [18]	7
Figure 1.3 a) Exhibition of Syngé's SNOM b) Main form of SNOM [21]	9
Figure 1.4 a) Aperture type SNOM b) Apertureless type SNOM (a-SNOM) tips [27].....	10
Figure 2.1 Calculation of electric field at the apex of probes with Different curvatures. Dimension of the probe's apex is decreasing from (a) to (f) [22]	13
Figure 2.2 Electric field's vector plot of a conductive spheroid by applying constant electric field along the spheroid [45]	18
Figure 2.3 Representation of the point-dipole model of a-SNOM probe [49].....	20
Figure 2.4 Schematic of the monopole model [47].....	23
Figure 2.5 Schematic diagram of self-homodyne detection	26
Figure 2.6 Schematic diagram of homodyne detection	27
Figure 2.7 Schematic Diagram of Pseudo-Heterodyne Detection	30
Figure 2.8 The oscillation of the reference mirror at frequency M in the pseudo-heterodyne detection [57]	31
Figure 2.9 Basis of higher harmonic demodulation [58]	32
Figure 3.1 Block diagram of communication VI which a) works for write and read data b) does not work for write and read data	35
Figure 3.2 Block diagram of SubVIs for main program.....	37
Figure 3.3 Block diagram of Timeout event.....	38

Figure 3.4 Block diagram of Save event.....	39
Figure 3.5 Block diagram of Clear event.....	39
Figure 3.6 Front panel of main program.....	40
Figure 3.7 Output spectrum of laser diode.....	41
Figure 3.8 A photomultiplier's components [60]	42
Figure 3.9 Nanopositioning system	43
Figure 3.10 Optical microscope image of attaching tuning fork with tip (probe)	45
Figure 3.11 Tip of the tuning fork mounted on nanopositioning system.....	46
Figure 3.12 Setting variables picture of MadPLL software.....	47
Figure 4.1 Schematic diagram of our self-homodyne detection setup.....	49
Figure 4.2 Photo of our optical setup.....	50
Figure 4.3 Photo of our electrochemical etching setup.....	51
Figure 4.4 Optical microscope images of first tungsten tip a) before electrochemical etching process b) after electrochemical etching process.....	52
Figure 4.5 Optical microscope images of second tungsten tip a) before electrochemical etching process b) after electrochemical etching process	52
Figure 4.6 Tip profile of first etched tip (app. 4–5 μm).....	53
Figure 4.7 Graph of near-field signal with first etched tip at first harmonic	54
Figure 4.8 Graph of near-field signal with first etched tip at second harmonic	55
Figure 4.9 Graph of near-field signal with first etched tip at third harmonic	55
Figure 4.10 Graph of the detected harmonic of near-field signals where all are together.....	56
Figure 4.11 Tip profile of second etched tip (app. 1 μm)	57
Figure 4.12 Graph of near-field signal with second etched tip at first harmonic	58
Figure 4.13 Graph of near-field signal with second etched tip at second harmonic.....	58
Figure 4.14 Graph of near-field signal with second etched tip at third harmonic	59

Figure 4.15 Graph of the detected harmonic of near-field signals where both are together.....	59
Figure 4.16 Different demodulation harmonics of near-field amplitude images using Au electrode on LAO/STO as a sample of pseudo-heterodyne detection [64]	60
Figure 4.17 Graph of measuring MoS2 with a-SNOM setup	62
Figure 5.1 THz-time domain spectroscopy schema. The sample is measured in the middle of the two PE lenses [73]	64
Figure 5.2 Schematic diagram of small probe beam path near-field detection setup in THz-TDS.....	66
Figure 5.3 Schematic diagram of long probe beam path near-field detection setup in THz-TDS.....	66

CHAPTER 1

INTRODUCTION

Researchers have been interested in the fabrication and characterization of nanometer-scale structures for long, and have continued to work on this subject with insistence. According to the definition by the National Nanotechnology Initiative, nanoscience research aims to discover new behaviors and properties of materials with dimensions at the nanoscale, a length scale of less than 100 nanometers (nm). Scientists have shown a willing interest in this regime's systems such as Drug-Delivery Techniques, Water-Filtration Techniques, Nanofilms, Nanotubes, Nanoscale Transistor, and Solar Plastics [1,2].

Overall spatial resolution is a common problem for most optical experiments. Atomic distance would commonly be in the range of a few angstroms; at the same time, the diffraction limit of light restricts the spatial resolution roughly by $\lambda/2$ [3]. Thus, having an instrument with spatial resolution lighter than the length scale of the systems under study is fundamental to measuring matter on the nanoscale.

The modern techniques being developed measure the spatial distribution of matter on nanoscale systems under the atomic radius resolution; these include the scanning electron microscopy (SEM) [4], scanning tunneling microscopy (STM) [5], atomic force microscopy (AFM) [6], transmission electron microscopy (TEM) [7], and X-ray spectroscopy [8].

All techniques which are mentioned above can give information about spatial distribution and limited electronic properties of the material [9]. Although, by using these techniques,

studying structural, optical, thermal, acoustic, and magnetic properties of materials are possible, it might be really troublesome experimentally. However, a successful and easy way has been found by researchers to study these materials' properties using light matter interactions [10].

To utilize light matter interactions to characterize materials, there are unnumbered techniques, including fluorescence measurements, conventional optical microscopy, and absorption measurements [11]. However, when an object becomes nanoscale in size, new physical effects appear and macroscopic rules change. Even though many techniques are developed in order to investigate and analyze nanometer phenomena, the diffraction limit of light is a limitation for the traditional optical techniques [1].

1.1. Diffraction Limit

Optical approaches for examining objects at high magnification have been extensively used in science and technology for many years. There are some outstanding advantages such as non-invasive measurement, high accuracy, easy to use, and so on. Technology is demanding a new characterization mechanism with higher spatial resolution to improve the nano realm. The traditional optical techniques have spatial resolution of about half the wavelength of the light source, known as the diffraction limit [1]. It specifies the upper limit of the smallest spatial properties that can be solved by both the imaging optics and the minimum spot size that a light beam can focus on [12].

In other words, the diffraction limit is when a point source is imaged by means of a finite aperture lens, and the light is spontaneously affected after passing through the aperture. Thus, the resulting image is not a point, but includes the diffraction pattern and it is known as an Airy disk [13]. E. Abbe has found that the smallest spot size that can be focused with an objective for the wavelength of light λ is

$$d = \frac{\lambda}{2n\sin\theta}, \quad (1.1)$$

Where,

d = the radius of the center spot of the Airy disk,

n = the refractive index of medium light,

θ = the collection angle of the objective,

$n\sin\theta$ = numerical aperture (NA).

L. Rayleigh has developed a specification for understanding the resolution easily.

Therefore, whereas the two Airy disks are still thought to be resolved under an optical microscope, the maximum separation between them should be at least equal to d . Contemporary high-resolution lenses have a very high numerical aperture, as large as 1.5. Given the aberrations and experimental circumstances, the objective lens' obtainable resolution is roughly calculated by using $\lambda/2$. For example, using a 500 nm visible wavelength as a light source and an oil immersion objective with a numerical aperture of 1.4, the feasible resolution will be approximately 250 nm. This is a major obstacle for the development of nanotechnology [1].

The light waves diffract based on the principle of Huygens. They generate constructive and destructive interference. The constructive interference is shown below [14].

$$d \sin \theta_m = m\lambda, \quad (1.2)$$

Where,

θ = the interference angle,

λ = the wavelength of light,

d = grating slit spacing,

m = an integer termed diffraction order.

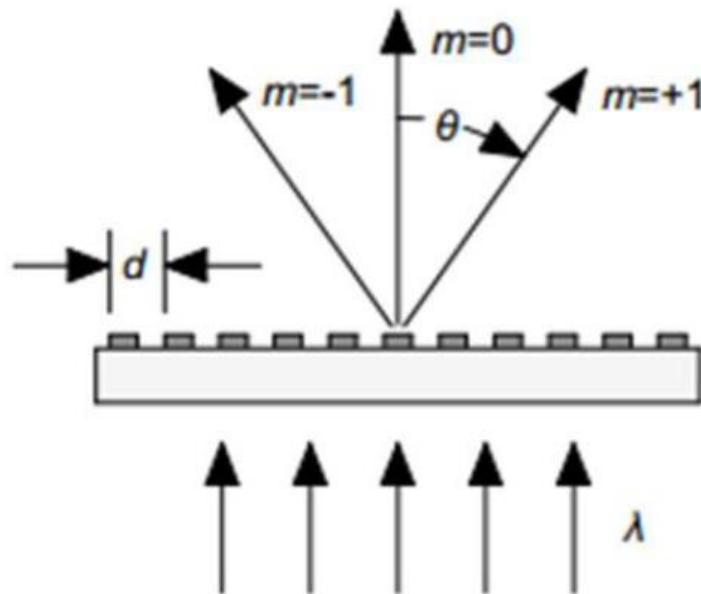


Figure 1.1 Light diffraction from a grating [15]

Two adjacent orders to resolve the grating, or the objective, must collect the zero-th order and at least one of higher order diffracted lights based on the Abbe's theory. This brings the following specifications:

$$\sin \theta \geq \kappa \cdot \sin \theta_1 = \frac{\lambda}{n \cdot d} \quad (1.3)$$

$$d \geq \kappa \cdot \frac{\lambda}{n \cdot \sin \theta} = \kappa \cdot \frac{\lambda}{NA} \quad (1.4)$$

Where,

θ = the collection angle of the objective,

θ_1 = the angle of first order interference,

d = the periodicity of grating,

n = the refractive index of medium between grating and objective,

NA = the numerical aperture of objective,

κ = a constant expressing quality of imaging system, which is 0.5 based on the criterion of Abbe.

Thus, both beam focusing and imaging resolution are delimited by the diffraction limit. Any measurement uses the far-field light to directly measure the spectroscopical properties of a sample. This evinces that it can never achieve a better spatial resolution than the diffraction limit [12]. However, the Fourier optics shows that any waves involve non-propagating components. At that rate, the lens only collects free propagation waves due to the macroscopic gap between the sample and the lens, even though it can collect the wave vectors from each angle. Thus, if the non-propagating components are collected, the diffraction limit can be overcome. This is possible with a-SNOM due to the near-field optics.

Scanning Near Field Optical Microscopy (SNOM) is the earliest way of beating the diffraction limit in optical microscopy. This microscopy serves if the evanescent waves are collected in the optical near-field region. These waves are associated with the subwavelength objects. Reaching the evanescent waves ensures high optical resolution. Another technique among scanning probe microscopy (SPM) techniques is SNOM, which started in different forms in the eighties [16].

There is a small tip that acts as a probe in SPM, indicating that a group of techniques are placed at a specific point on a two-dimensional sample, and are collected only from that specific point. This continuum has been repeated at every point on the two-dimensional sample surface to produce scientifically interesting material knowledge from that sample's spatial image. a-SNOM is one of the SPM techniques [12]. Thus, the a-SNOM technique can measure spectroscopic properties of samples on nanoscale which are smaller than the diffraction limit.

1.2. Scanning Probe Microscopy

The invention of scanning tunneling microscopy (STM) and atomic force microscopy (AFM) threw light about SPM. The SPM technique uses the principles of STM and AFM. These principles rely on utilizing of a probe and precise positioning of the relevant material to probe at nanoscale [17]. In other words, a novel approach to a surface within the atomic scale and to high-resolution microscopy is represented by the scanning probe techniques.

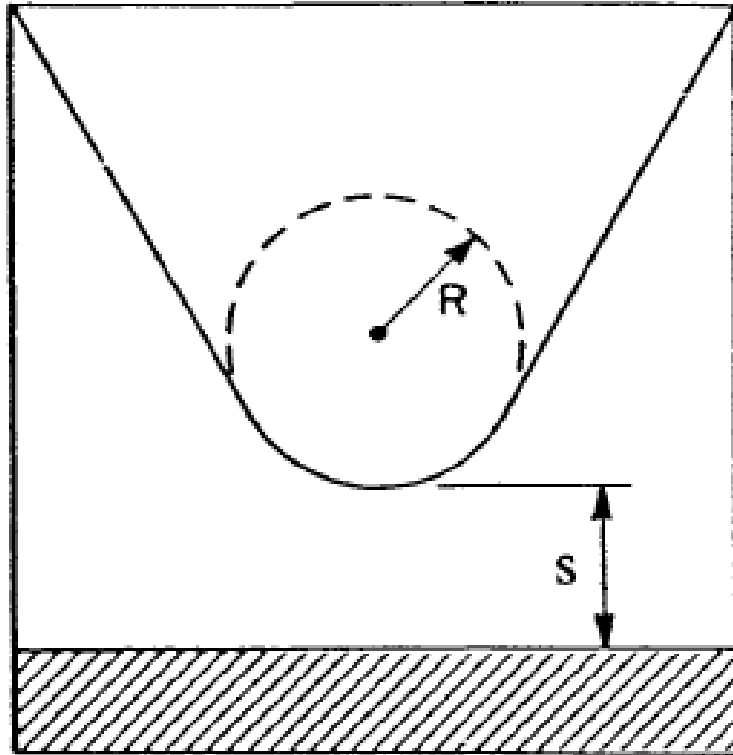


Figure 1.2 Scanning Probe Geometry [18]

According to the scanning probe technique, when the interaction between the tip and the sample takes place, a sharp probe brings in very close to the sample surface. The interaction localizes based on the probe tip's shape and the finite effective range's interaction spatially. Protecting the interaction strength at a constant pre-setting value with a feedback circuit can make use of address the tip at a finite tip-sample surface separation for the gap dependence of a specific tip-sample interaction. When the tip is raster-scanned over the sample's surface, the related characteristic of the material is registered at each pixel on the sample, and its characteristic associated with the tip's position with respect to the sample. Thus, generating the two-dimensional spatial image of the sample's surface property is possible by the SPM technique. Many properties are measured by using varied SPM techniques such as viscosity, sample topography, conductivity, and other electromagnetic parameters of the sample. The tip-

to-sample separation s is microscopically small and this separation is characteristically smaller than the wavelength λ of the specific interaction to be investigated, as a result of the characteristic of all scanning probe methods.

Thus, scanning probe microscopes have worked in the near-field (NF). Therefore, the spatial resolution is specified based on the tip-to-sample distance and the radius of the probe tip's curvature. This resolution is independent from the wavelength, even though it plays an important role for diffraction-limited resolution in the far-field (FF). STM is a one of the typical NF methods that presents a better spatial resolution than the wavelength of the electrons, which is a tunnel between the tip and sample. Similarly, using any scanning probe method in the NF regime could help explain any type of tip-sample interaction which provides a spatial resolution better than the diffraction limit [18]. Although the SPM family has a huge impact on science, they are important to new technologies. One example is manipulating and sensing the topography of a material's abilities at the nanoscale created new technology for high density data storage [19]. Modifying material biologically may be used for drug discovery [20]. Thus, SPM techniques also give a start to the increasing attempts in the development of SNOM. Various experimental methods actualize for performing SNOM. My goal is to build a practical version of a-SNOM. There are three main points for a-SNOM systems. These are holding the tip in the sample interaction region, measuring the height of the sample, and scanning the tip around the sample to generate a two-dimensional map of the topographic and spectroscopic structure of the sample, such as AFM [12].

1.3. The Development of SNOM

Looking at the different historical movements can outline the development of SNOM. While this conceptive design is actually quite old, it has been found as a result of Syngé's research in 1928. Thus, the near-field optical resolution concept beating the diffraction limit has been established by him [21]. The first experimental demonstration has been in the microwave regime in 1972; entering the optical regime has been achieved by the middle of 1980s. Pohl et al. and Lewis et al. have realized the near-field measurement at visible wavelength separately, achieving spatial resolution better than $\lambda/10$. [22]

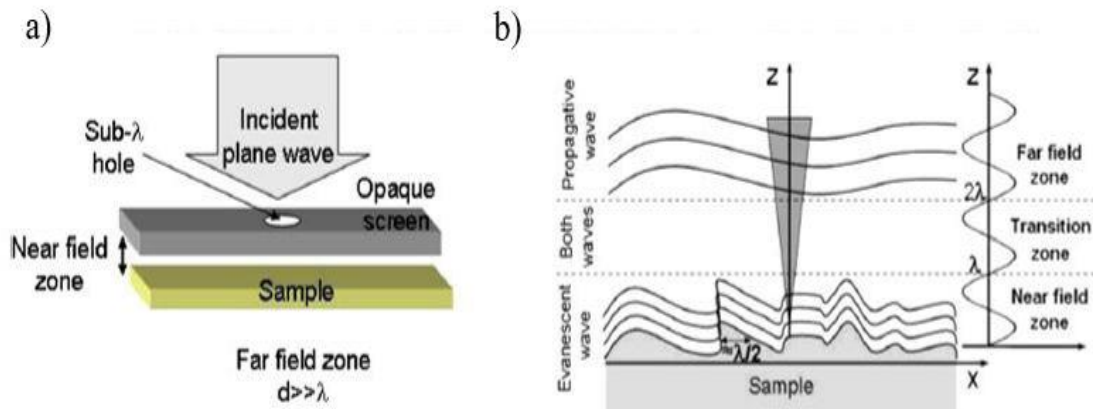


Figure 1.3 a) Exhibition of Syngé's SNOM b) Main form of SNOM [21]

A significant achievement has happened by the invention of new SNOM probes. By then, the near-field optical microscopy has grown consistently. A new type of SNOM probe, by forming the aperture at the end of a metal-coated tapered single mode optical fiber, was created in 1991 [23]. Controlling the probe and sample distance with the tuning fork technique has been advanced four years later by Karrai and Grober [24].

This tuning fork technique has turned into a well-known mechanism for aperture-type SNOM. The photon scanning tunneling microscopy (PSTM) or the scanning tunneling optical

microscopy (STOM) has been created as another type of SNOM by Courjon et al. in 1989 [25]. The evanescent field is detected by using sharp optical fiber in the reflection mode. This technique is utilized in many applications in the field of optical waveguides and propagation of surface plasmon polaritons. Whereas the aperture type of SNOM is improving continuously, Synge's initial idea revealed the apertureless SNOM (a-SNOM) or scattering type of SNOM (s-SNOM) using light scattered by a small particle as a light source. The first prototype has been guided in 1989 by Fischer and Pohl [26].

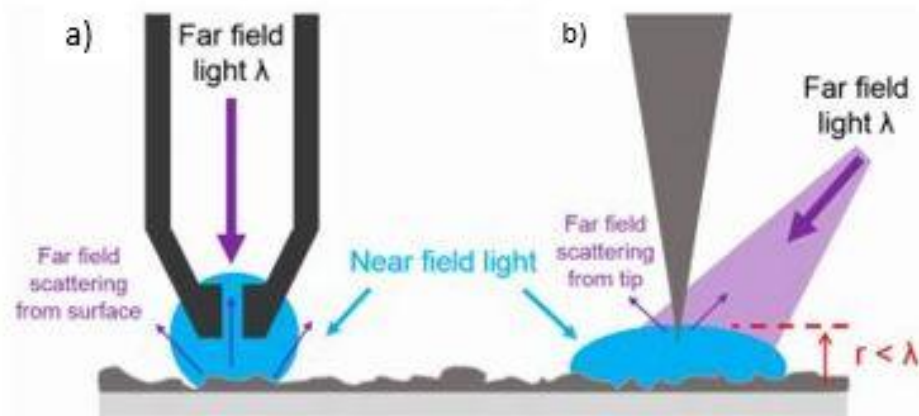


Figure 1.4 a) Aperture type SNOM b) Apertureless type SNOM (a-SNOM) tips [27]

The desired near field signal come from scattering from a subwavelength region of optical tip-sample interaction in a-SNOM. Gerton et al. have indicated that the spatial resolution is only limited by the tip radius, which is generally below 15 nm [28].

The light is scattered not only from the sample, but also from the tip. Because of this reason, the near-field signal contains undesired far-field background. The beating overwhelming far-field background signal has been obtained by suppressing the background. The only way to detect as much as a pure near-field signal is possible by dithering the tip on vertical direction

with frequency Ω and demodulation at higher harmonics $n \Omega$ [28,29]. Throughout the development of SNOM, it has also been realized that the laser radiated from the metal tip has so strongly enhanced optical intensity, which is more than that of the excitation source, when the incident field is polarized along the tip shaft. This strong scattering scheme has been further developed in spectroscopy – for example, the tip-enhanced fluorescence microscopy and tip-enhanced Raman spectroscopy [1].

CHAPTER 2

A-SNOM THEORY AND MEASUREMENT TECHNIQUES

Nanometer scale materials' property of optical response can test the effectiveness of classical electrodynamic notions which are usually employed in nano-optical investigations. As an example, when geometrical restrictions smaller than the free electron path cause increased scattering of free charge carriers, the bulk dielectric constants of metals are not appropriate [31,32]. Because of this conflict, ascertainment of analytical result may not be possible. Besides this, the simplest and idealized geometric shapes like a plane or a sphere, and ideally uniform material properties can be obtained [33]. When the diameter of aperture can be below $\lambda/2$ on the aperture type SNOM, the propagation of light would be evanescent [34]. A very small aperture, which is less than 50 nm, makes it impossible to work under visible wavelengths. Beating this wavelength dependent resolution limit, another type of SNOM called a-SNOM is created as an alternative to light transmitted through a small aperture, for the enhanced field around the small particle utilizes an optical nano source. In this way, the near-field signal of probe-sample interaction can carry information about the sample, while this is measured in the far-field by a-SNOM system [1].

2.1 Confinement and Enhancement of Field

High level enhanced field at the apex of the probe has made a-SNOM incredibly skilled in precision measurements. Under this circumstance, the near-field interaction among the probe and sample is adequately strong for detecting signals in the far-field [35,36]. The accomplishable

resolution is designated by the a-SNOM probe's curvature radius. In addition to this, the field enhancement is forceful enough to influence the scattering signal into the far field beneath the probe. Wherefore reaching the 10–20 nm sharp radius of curvature probes are typically available, the optical resolution below the conventional diffraction limit can be attained.

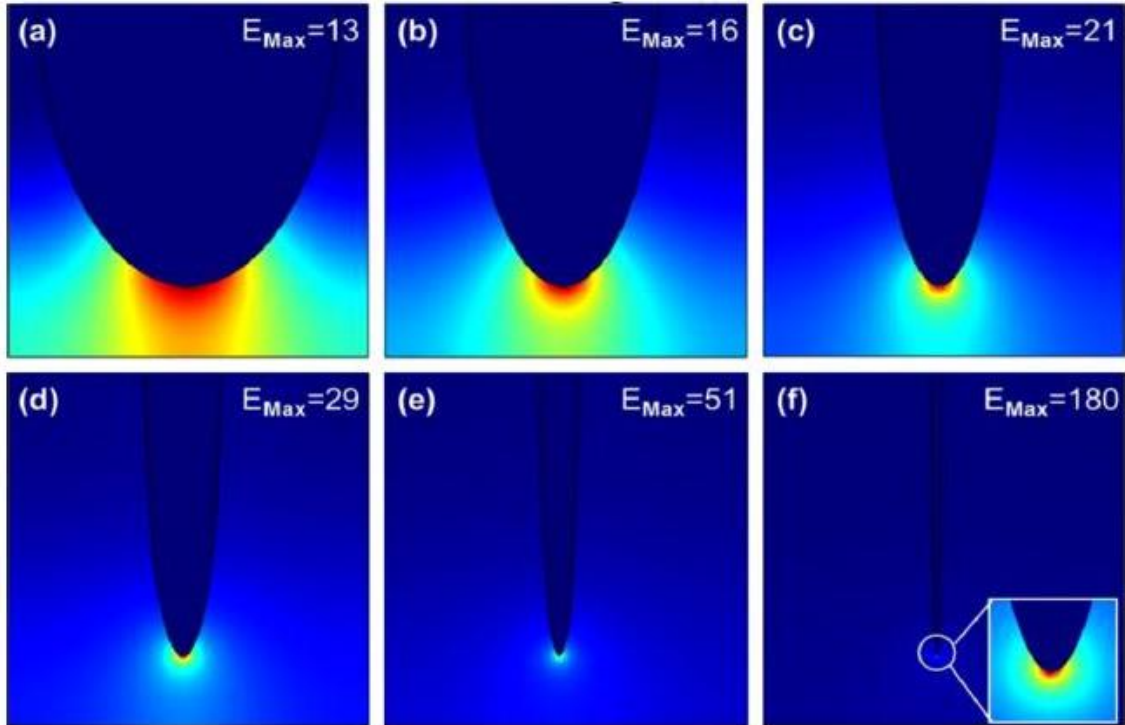


Figure 2.1 Calculation of electric field at the apex of probes with different curvatures. Dimension of the probe's apex is decreasing from (a) to (f) [22].

The application of a-SNOM is similar to an AFM system. Radiation light is focused onto the apex of an AFM tip. Then, the strongly localized field composed in its surrounding area is used to probe the optical property of a sample. While collecting topographic information of the sample, an optical map will be simultaneously acquired by doing the AFM scans. Similarly, the key aspect of s-NSOM is that the highly confining and enhancing field is near the apex of the AFM tip. As a result of this, the radius of the tip curvature states the field confinement, which

specifies the lateral resolution [37]. The following subject will cover some ideas on where the enhancement generally comes from.

2.1.1 Lightning Rod Effect

The probe's geometry leads to the large field enhancement, which is based on the effect of the lightning rod [38]. The free electrons oscillating along its length is compelled by incident light polarized along the axis of the probe. When many electrons are brought together at the end of the apex of the probe, the high charge density has been created. This causes a broad, extremely confined electric field with enhancement features usually in the hundreds [32]. It does not have any wavelength dependence purely due to a shape effect. As the incident light polarization is perpendicular along the probe's axes, the lightning rod effect has been much dropped and the near-field measurement has been less impressionable [39].

A simple demonstration of this effect is to examine a dielectric sphere in the static electric field. A quasi-static approach can be made, supposing that the diameter of the sphere is much smaller than the wavelength. In order to solve the electric field distribution inside and outside the sphere, Maxwell's equation at boundary of sphere is applied from the book of electrodynamics [40].

$$E_{out}(r, \theta) = E_0 \cos \theta \left(1 + 2 \cdot \frac{\frac{\epsilon}{\epsilon_0} - 1}{\frac{\epsilon}{\epsilon_0} + 2} \cdot \frac{a^3}{r^3} \right) \cdot \hat{r} + E_0 \sin \theta \left(-1 + \frac{\frac{\epsilon}{\epsilon_0} - 1}{\frac{\epsilon}{\epsilon_0} + 2} \cdot \frac{a^3}{r^3} \right) \cdot \hat{\theta} \quad (2.1)$$

$$E_{in}(r, \theta) = E_0 \frac{3}{\frac{\epsilon}{\epsilon_0} + 2} (\cos \theta \cdot \hat{r} - \sin \theta \cdot \hat{\theta}) \quad (2.2)$$

Where,

a = the radius of the sphere,

E_0 = the applied uniform field,

ε = the permittivity of sphere,

ε_0 = the permittivity of environment medium.

According to the result, on the one hand, the field inside the dielectric sphere is of uniform feature, and its direction is the same as the applied field's direction. On the other hand, a superposition of the applied field and the electric dipole's field gives the outside of the sphere's field. There would be field enhancement near the sphere surface along the direction of polarization, due to the fact that it is superposition of the outside field [41, 42]. This shape of elliptical spheroid exists in a uniform external electric field at the polarization of the major axis. The field distribution might be analytically calculated based on the electrostatic approximation. According to Ermushev et al. [43], the local electric field E_{loc} at the bottom tip of the spheroid is

$$E_{loc} = \frac{\varepsilon E_0}{1 + (\varepsilon - 1) \cdot A'} \quad (2.3)$$

Where,

$$A = 1 - \xi Q_1'(\xi)/Q_1(\xi) \text{ and } \xi = a/(a^2 - b^2)^{1/2},$$

a = the semi-major axis,

b = the semi-minor axis ($a, b \ll \lambda$),

Q_1 and Q_1' are called the Legendre function of the second kind and its derivative respectively.

Proportion of E_{loc}/E_0 has qualified the field enhancement from the equation. Identifying the enhancement of field is attributed to two factors – the ellipsoid depolarization factor A and the dielectric function of the spheroid. It has been realized that A is only a geometrical factor

based on the axis ratio a/b of the spheroid. As the ratio a/b soars – in other words, a higher curvature at the ends of the spheroid – the factor A tends to be smaller and the field enhancement will be higher. This has verified that the lightning rod effect has a role in the field enhancement.

2.1.2 Optical Antenna Effect

The conversion between the field localization and the propagation of electromagnetic waves is arisen from the optical antenna. The antenna for radio or microwave frequency can be given as an example. When the length of radio antenna changes, it can help attain high efficiency basically. According to the electrodynamic calculation, the optical antenna effect in field enhancement of a sharp tip is quantified with utilizing the elongated spheroid as similar to the SNOM probe tip [41,44]. Hereby, the enhancement field at the end of a sharp tip apex is accomplished with assistance from the effect of extensive optical antenna. This effect is linked to the light's wavelength, the axis ratio of spheroids, direction of the incident optical polarization and excitation [41].

2.1.3 Localized Surface Plasmon Resonance

Localized surface plasmon resonance may also play a role in the field enhancement at the probe apex. The reason for the major field enhancement may be plasmon resonance for metal tips working with visible wavelengths. The collection of oscillating electrons has generated the plasmon resonance. Therefore, localized surface plasmon effect differs from antenna effect. The field enhancement would alter with specific dielectric functions based on the spheroid model. Thus, the induced electrons' oscillation can have little damping which causes local surface plasmon excitation. It is easily noticed that the plasmon resonance has enhanced the field at the apex. However, it can be informed that the resonance relies on the tip shape and the tip-sample separation. Therefore, explication of the experimental result is obstructed [1].

2.2 Theoretical Models for Tip-Sample Interaction

The a-SNOM uses sharp tip as an antenna to replace the near field in the close proximity of the sample into measurable optical signals, which can be called scattered near-field signal. A quantitative model of the near-field interaction between tip and sample will provide a key to precise material identification according to the near-field spectra and optical resonances. The field confinement and enhancement in the vicinity of tip apex have provided the ability of a-SNOM to achieve high resolution and a plausible signal level. Moreover, the process of image creation should be understood in order to provide information from measured results. Although numerical studies of the near-field interaction between the tip and sample operate different computational techniques, an analytical model will help to understand the contrast mechanism and the signals' root. The intensity of the scattered near-field signal has carried the amplitude and phase information of the near field. As the shape complexity of a-SNOM probe has obtained an analytical result, simplifying the problem should be necessary. That is why considering the conical or pyramidal shape of s-NSOM probe and the nature of near-field interaction are important in order to model the interacting apex of tip by its resemblances such as a sphere or spheroid. For this reason, the probe shaft has less impact on near-field interaction. Thus, the shaft of probe effect is often neglected to simplify the problem. The sample, the distance between the tip and the sample, and the dielectric function of the tip have huge effects on the scattered near-field intensity in a-SNOM. Although there are some different theoretical models for the a-SNOM tip-sample interaction, I will consider the prolate spheroid model, the point dipole model, and the monopole model. Once and for all, the following models have used the quasi-static approximation.

2.2.1 Tip Spheroid Model

The tip has been patterned as a dielectric prolate spheroid, conducting in the tip spheroid model. While this model considers about the tip, it has ruled out the sample in its applications.

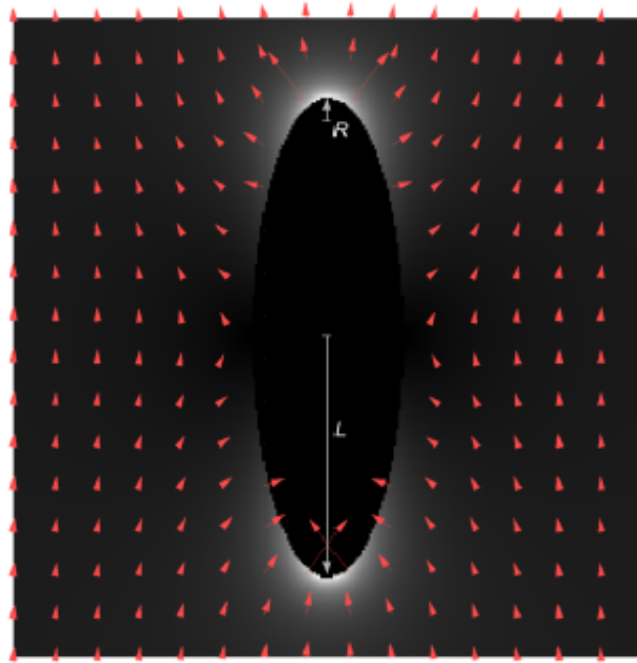


Figure 2.2 Electric field's vector plot of a conductive spheroid by applying constant electric field along the spheroid [45]

Maxwell equations have been used to solve the spheroidal geometry model. The electromagnetic calculation does not make it difficult to analyze this method. The incident laser field has been taken constant and the uniform electric field is valid [41]. It is necessarily noted that the homogeneous field can be represented as an illumination if the spheroids are much smaller than the wavelength [46,47,48].

The spheroid and this electric field affect each other. As a result of this interaction, the electric field takes place enhancement at close proximity to the top and bottom of the spheroid. The reason is that the electric field directs a charge separation in the spheroid, and a charge

accumulation occurs at high curvature points on the surface, which leads to a large field enhancement. As I mentioned before, this is known as the lightning rod effect.

The distance dependency of this field enhancement may be explained as an electrostatic calculation [47].

$$E_s(z) = \frac{\frac{2F(L+z)}{z^2 + L(2z+R)} + \ln \frac{L-F+z}{L+F+z}}{2 \frac{F(L-\epsilon_t R)}{LR(\epsilon_t - 1)} - \ln \frac{L-F}{L+F}} E_0 \quad (2.4)$$

Where,

F = the distance from the center of the spheroid to a focus,

L = the length of the major axis of the spheroid,

R = the radius of curvature at the apex,

z = the distance from the apex of the spheroid,

ϵ_t = the dielectric constant for the spheroid,

E_0 = the incident electric field.

Although the spheroid model is very well represented for the apex of tip, it does not express the long range spatial extent of the tip. Another limitation of this model is that the analytical solution is not enough because of the absence of the dielectric sample.

2.2.2 Point Dipole Model

The point dipole model has two main simplifications. First of all, it is supposed that the apex of the a-SNOM probe plays a role in the near-field interaction with the surface of the sample. For this reason, it is approximately accepted the probe is a small sphere. Secondly, the illuminating light has produced the dipole of the tip. This is presumed infinitely small and located at the sphere's center [49].

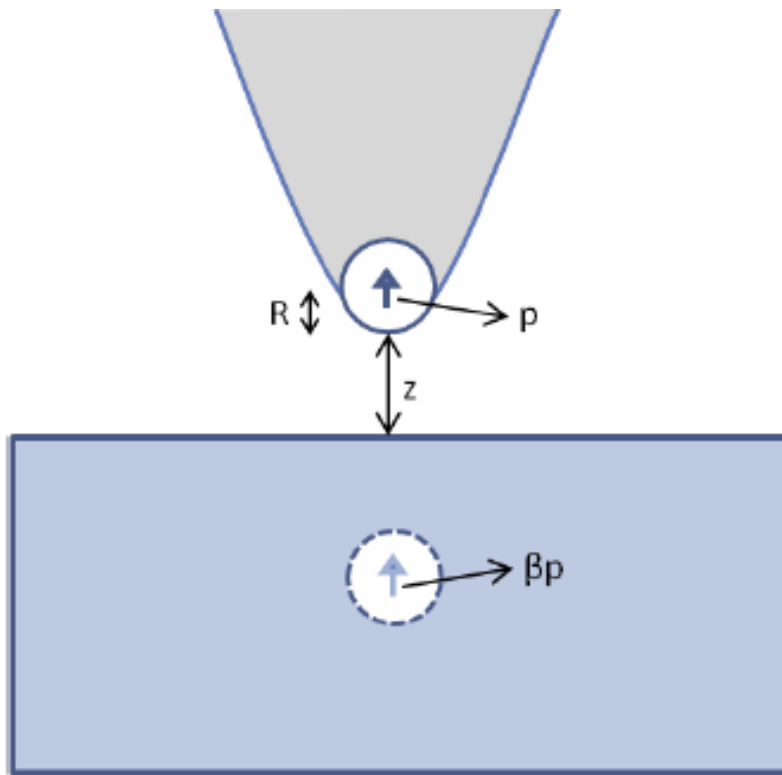


Figure 2.3 Representation of the point-dipole model of a-SNOM probe [49]

The tip of the a-SNOM system behaves as a polarizable sphere with radius R in the point dipole which is the simplest model of the tip-sample interaction [39]. The sample is a half space plane with a complex dielectric constant ϵ_{tip} . It can be either dielectric or metallic [29]. As the electric field has exposed this system, a dipole is excited by the field in the tip sphere. The fact that an image dipole is excited in the sample due to the dielectric nature of the sample surface

cause that this coupled dipole system holds an effective polarizability α_{eff} . The oscillation of electric field (E_{inc}) has combined with this polarizable system, which relies on the results in a total electric field with amplitude where E_{tot} is proportional to $\alpha_{\text{eff}}E_{\text{inc}}$. The dipole couple system scatters this electric field which provides ratio $E_{\text{sca}} / E_{\text{tot}}$ scattered into the far field to be detected. Thus, it may be seen that α_{eff} relies on the dielectric constants for both the tip and the sample, ϵ_{tip} and ϵ_{surf} , the tip-sample separation, z . Moreover, the importance of the direction of polarization can be realized when the incident electric field is polarized parallel to the tip axis, p-polarized, or perpendicular to the tip axis, s-polarized. The following equations have been shown by this model [39].

Polarizability of a dielectric sphere:

$$a = 4\pi R^3 \left(\frac{\epsilon_{\text{tip}} - 1}{\epsilon_{\text{tip}} + 2} \right) \quad (2.5)$$

Relative strength of the image dipole:

$$\beta = \frac{\epsilon_{\text{surf}} - 1}{\epsilon_{\text{surf}} + 1} \quad (2.6)$$

Effective polarizability of sphere coupled to image sphere for p-polarized light:

$$\alpha_z = \alpha \left(1 - \frac{\alpha\beta}{16\pi(R+z)^3} \right)^{-1} \quad (2.7)$$

Effective polarizability of sphere coupled to image sphere for s-polarized light:

$$\alpha_x = \alpha \left(1 - \frac{\alpha\beta}{32\pi(R+z)^3} \right)^{-1} \quad (2.8)$$

As a result, the scattering efficiency of the tip builds upon the magnitude of the tip dipole which comes out of this polarizability. When the incident light polarization is parallel to the surface, the image dipole is also parallel. However, looking at the opposite direction, it is leading to a partial cancellation of the total dipole moment [50]. It is noticeable that the p-polarized light field enhancement is higher than the s-polarized light, due to the fact that a-SNOM works with light polarized throughout the axis of the tip. This can be logical from the viewpoint of the antenna. It is seen that charges are move more in the z direction than the x or y directions. Besides this, the s-polarization light can also be used in some situations [51]. It may be seen clearly that the scattered signal includes information of the tip, the sample, and about the distance between sample and tip. Therefore, when the distance between tip and sample stays constant and the tip doesn't change during the scanning process, fluctuation in the scattered intensity should be because of local changes in the dielectric constant of the sample [52, 53,54]. Although the point-dipole model has some advantages and is effective, it has shown drawbacks also. One of the important drawbacks of the dipole model is weak numerical agreement. The experimental and exact models have not been matched.

2.2.3 Monopole Model

The monopole model is analogue to the simple dipole model, but the tip is modelled as an extended spheroid. Analytic electric field calculations throughout the prolate spheroid has generated the extended dipole model. Additionally, the prolate spheroid is exposed by a constant electric field. This model has worked as the interaction of incident field interacting with the dielectric functions of the tip and the sample. It stands separate from other models by inducing image charges in the sample [45]. The calculation has proved that the field of extended charge distribution is more valid than the field of point dipole [41].

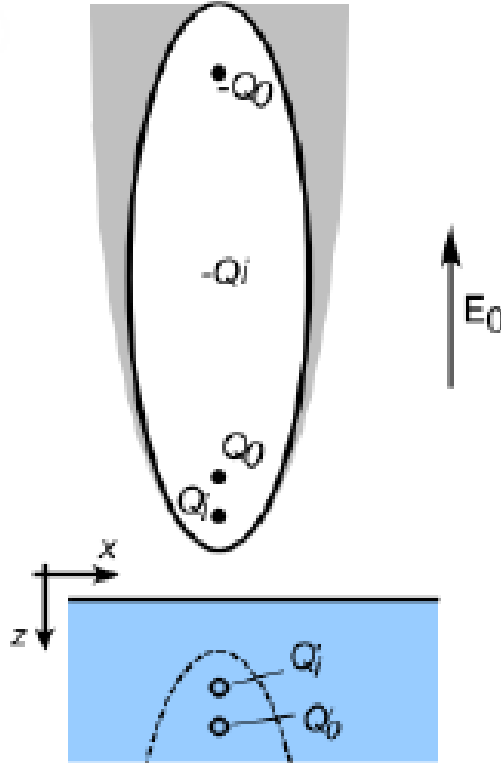


Figure 2.4 Schematic of the monopole model [47]

According to the simple dipole model, driving a dipole which pinpoint in the sphere's center happens when the effect of the electric field occurs on the tip. On the other hand, the electric field drives a charge separation in the extended dipole model. Because of this effect, Q_0 may be found at the tip apex, and negative Q_0 may be found far away from the apex up the tip shaft. Since only charges near to the sample surface will contribute towards interaction, $-Q_0$ will not be taken into consideration. Thereby, Q_0 leads to a mirror charge effect Q_0' in the sample surface. Then, the mirror charge effect will reallocate the charges on the tip. To approximately calculate the reallocated charge, the approximation replaces the spheroid with another monopole charge Q_i . Again, another mirror charge Q_i' shows up on the sample surface. Calculations are conducted on this interaction; thus, its recursive nature is captured. This process facilitates an effective polarizability and values to be formed for Q_0 and Q_i .

The ensuing expression is for the scattered near-field distance dependence as shown below [47].

$$\alpha_{\text{eff}} = R^2 L \frac{\frac{2L}{R} + \ln \frac{R}{4eL}}{\ln \frac{4L}{e^2}} \left(2 + \frac{\beta \left(g - \frac{R+z}{L} \right) \ln \frac{4L}{4z+3R}}{\ln \frac{4L}{R} - \beta \left(g - \frac{3R+4z}{4L} \right) \ln \frac{2L}{2z+R}} \right) \quad (2.9)$$

Where,

R = the tip radius,

L = the length of the semi-major axis of the spheroid,

β = the reflectivity of the sample,

g = a parameter related to distribution of the induced electric charges,

z = the tip-sample separation.

Since this analytical theory enables to catch more quantitative features of the interaction in comparison with the simple dipole model, it is useful. Although the expressions are quite complex themselves, the extended dipole model presents more parameters than the simple dipole model. That is why the better fit is expectable. The extended dipole and the simple dipole models are shown as perfect through experimental results. However, they are restricted like all other theoretical models. As an example, both models presume an infinite dielectric plane for the sample. But, the shape of the tip apex may be differing from the real shape for both the models [12].

2.3 Near-Field Signal Detection Techniques

Although a-SNOM has provided many advantages, detecting the pure near-field signal is really difficult. The large scattering background signal is seen from the sample surface and the reflections of the probe shaft. This is problematic because the scattering background signal does

not carry information about the sample during the near-field interaction and it affects the radiation which goes to the detector. During the development of a-SNOM, various ways are devised for suppressing undesired background radiation. One of them is modulating the tip-sample gap and demodulating at higher harmonics, which have been successful to separate background from pure near-field signal [55].

In order to increase the near-field signal intensity, interferometric amplification techniques are proposed. The principle behind the interferometric technique is that the near field (E_{nf}) beam interferes by a constant higher intensity amplification beam (E_{amp}). This interferometric technique is that obtaining a new term is instantly proportional to E_{nf} multiplied by E_{amp} . Then, the large E_{amp} factor calibrates the near-field signal's information.

$$\begin{aligned}
 I_{det} &\approx E_{tot}E_{tot}^* = (E_{nf} + E_{amp})(E_{nf}^* + E_{amp}^*) \\
 &= E_{nf}^2 + E_{amp}^2 + (E_{nf}^*E_{amp} + E_{nf}E_{amp}^*) \quad (2.10) \\
 &= E_{nf}^2 + E_{amp}^2 + 2|E_{nf}||E_{amp}|\cos(\Delta\varphi)
 \end{aligned}$$

There is a phase difference between the amplification field and the near field. " $\Delta\varphi$ " shows this phase difference. In the last equation above, magnitude of the E_{nf}^2 term is very small. This reason makes it negligible. The lock-in amplifier cannot detect the second term (E_{amp}^2) because it has not taken part at frequencies $n\Omega$. Thereby, the last term of the last equation determines the measured signal. It has been shown as the signal based on the near-field information multiplied by the strength of the amplification field and the optical phase difference ($\Delta\varphi$).

Different interferometric detection schemes have been proposed to extract the pure near-field interaction. These are the self-homodyne method, homodyne method, and pseudo-heterodyne method; the three methods rely on the nature of the amplification field (E_{amp}) [12].

2.3.1 Self-Homodyne Detection

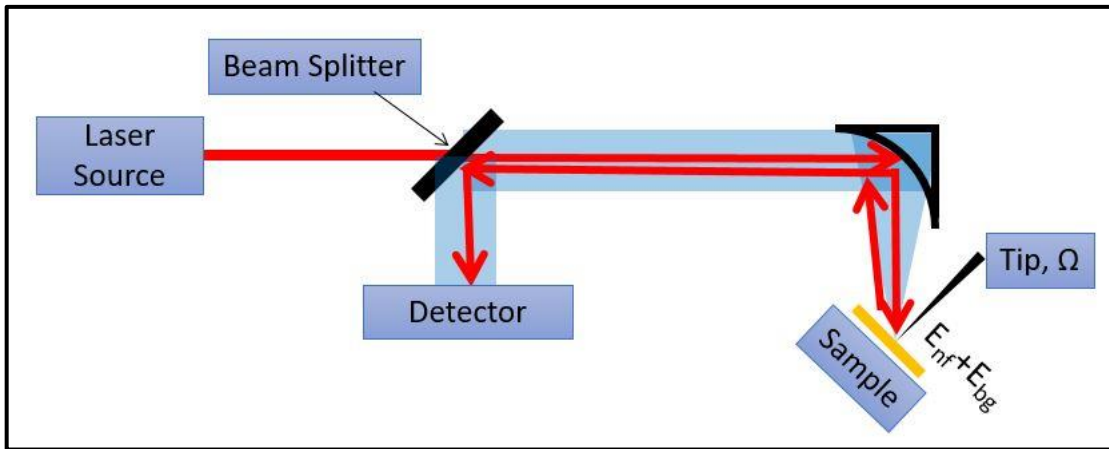


Figure 2.5 Schematic diagram of self-homodyne detection

The optical reflections from sample and tip which compose the background field is generated by the amplification field in self-homodyne detection. The scattered near-field light (E_{nf}) interferes with the background light scattered from the sample (E_{bg}) to boost the low intensity near-field signal. Moreover, the cuddling of the near-field amplitude and phase image is provided by self-homodyne detection. The reflected (E_{bg}) field displaced of (E_{amp}).

Self-homodyne detection, which is the simple scheme of the interferometric detection, is used to measure many near-field measurements. On the other hand, this detection method also include major limitations. As an example, E_{bg} mainly emerges from (spatially) random scattering cases. Thereupon, this effect causes an uncontrollably varying magnitude depending on where the tip is located with respect to the sample. Moreover, although E_{bg} is spatially continual, it is not continual in terms of phase.

The factor of $\cos(\Delta\phi)$ causes that as near-field signal phase is continual, the measured image would necessarily image the background signal's phase. This image would display bright and dark interference fringes with spatial frequency on the order of the incident light's wavelengths (λ) [56].

Note that the amplification field's phase and amplitude cannot be controlled because many artifacts such as interference fringes and topographical artifacts have an effect on the image. Besides this, the near-field signal consists of not only amplitude but also phase information. However, the self-homodyne detection measurement enables only one value which includes amplitude and phase of the near-field together [12].

2.3.2 Homodyne Detection

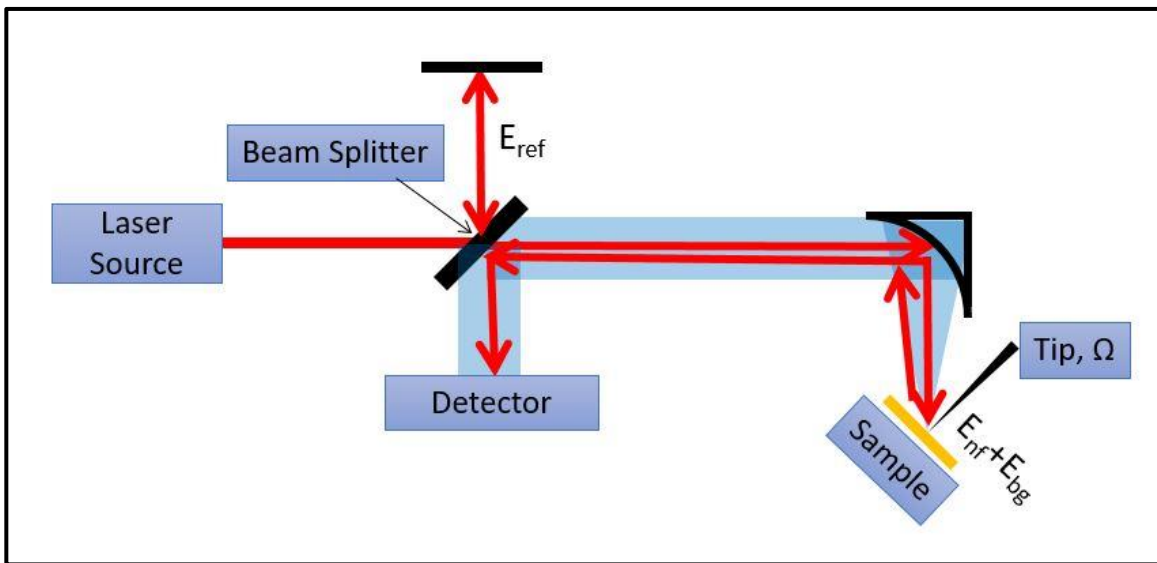


Figure 2.6 Schematic diagram of homodyne detection

The reference beam (E_{ref}) has substituted the amplification beam (E_{amp}). That reference beam cannot go through the sample beam path because of the beam splitter. Then, it reflects back like in the Michelson interferometer. In this way, three main beams (E_{nf} , E_{bg} , and E_{ref}) reach the

detector, interfering each other. Understand that using a controllable reference beam will help reduce the effect of background artifacts.

The following interference equations are shown:

$$\begin{aligned}
I &\approx E_{tot}E_{tot}^* = (E_{nf} + E_{bg} + E_{ref})(c. c.) \\
&= E_{nf}^2 + E_{bg}^2 + E_{ref}^2 \\
&\quad + E_{bf}E_{ref}^* + E_{bg}^*E_{ref} \\
&\quad + E_{nf}E_{bg}^* + E_{nf}^*E_{bg} \\
&\quad + E_{nf}E_{ref}^* + E_{nf}^*E_{ref}
\end{aligned} \tag{2.11}$$

When numerically examining these equations, since the first term of the equation above has a small magnitude, it is inconsequential overall. And then, the following four terms also are not consequential: They are not related with E_{nf} . In addition to this, these four terms are not modulated by the tip oscillation frequency's harmonics. That is why the lock-in amplifier cannot detect these terms. Known that E_{ref} is much bigger than E_{bg} , it has made the following two terms likely to be inconsequential. Finally, after revising the equation, it is written again as shown here:

$$I \approx 2|E_{nf}||E_{ref}| \cos(\Delta\varphi) \tag{2.12}$$

Where, $\Delta\varphi$ represent the relative phase between the near field light and the reference beam.

When E_{ref} changes with E_{bg} , the equation above is same as the equation for detected intensity. The main assistance of homodyne detection is that the magnitude of E_{ref} is stable. This happens because of three reasons. Firstly, the reference beam comes precisely from the source of laser. Secondly, it is simply a reflection beam. As a third reason, the beam path length does not change in time. Therefore, the phase difference $\Delta\varphi$ is also stable.

Displays that make the measurement at two different $\Delta\phi$ values enable to determine the proportional to the magnitude of $|E_{nf}|$ and $\Delta\phi$ value together. When considering two measurements with different values of phase difference such as $\Delta\phi$ and $(\Delta\phi - (\pi/2))$, the equation is obtained as shown below.

$$\begin{aligned}
 I_1 &\approx 2|E_{nf}||E_{ref}|\cos(\Delta\phi) \\
 I_2 &\approx 2|E_{nf}||E_{ref}|\cos\left(\Delta\phi - \frac{\pi}{2}\right) = 2|E_{nf}||E_{ref}|\sin\Delta\phi \\
 I_1^2 + I_2^2 &\approx |E_{nf}|^2 \\
 \arctan\left(\frac{I_2}{I_1}\right) &= \Delta\phi
 \end{aligned} \tag{2.13}$$

This is obtained by following calculations at single point for two measurements; it can enable to detect the magnitude and phase values of the near-field signal at a specific point. Thus, continuing through all points of sample, the image is created to realize spatial near-field optical contrast in not only magnitude but also phase.

It is seen that the homodyne detection has more features than the self-homodyne detection. As an example, it gives more information about the sample. Moreover, the higher quality of signal-to-noise ratio and the optical contrast are obtained within the interferometric detection schemes by the homodyne detection [12].

2.3.3 Pseudo-Heterodyne Detection

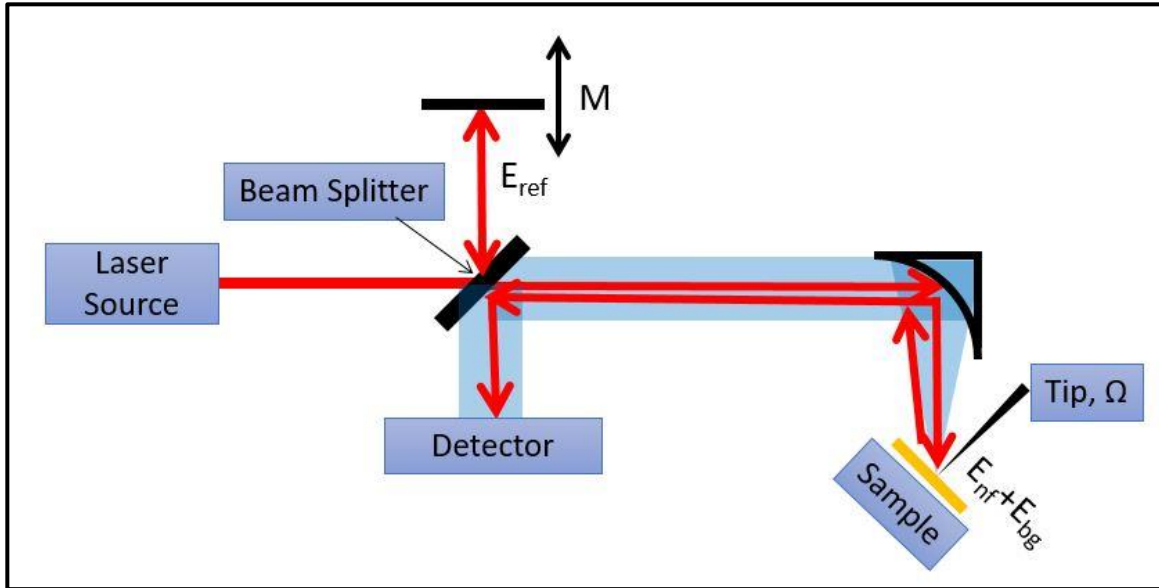


Figure 2.7 Schematic Diagram of Pseudo-Heterodyne Detection

The pseudo-heterodyne detection method has been proposed to magnify the small near-field signal. A configuration of this setup is known specially as the Michelson interferometer [57]. The idea behind this interferometric detection is that it modulates the phase of reference wave to interfere with the near-field scattering signals. So, it does not utilize a reference light of different frequency for interfering with the near-field scattering signal.

The incident beam is reflected by a mirror to interfere with the tip scattered light after splitting the beam at the beam splitter for using as a reference beam. An additional component, $\gamma \cos(Mt)$, represents the incident beam's phase because the mirror has sinusoidal oscillating, which creates the phase of incident beam [58]. Hereby, the phase modulated reference wave is shown in the following equation.

$$E_{ref} = |E_{ref}|e^{-i\omega t + i\gamma \cos Mt} + c. c. \quad (2.14)$$

Where,

M = the phase modulation frequency, which is the reference mirror's frequency,

γ = the modulation depth of the reference mirror oscillation.

According to the calculation by Ocelic et al. [57], when this reference beam interferes with E_{nf} , each peak at frequency $n\Omega$ is split into sidebands, which is separated by frequency M . As the detector measures intensity proportional to E^2 , it stirs the two signals at frequencies Ω and M . Thus, the signal is detected at frequencies $n\Omega + mM$.

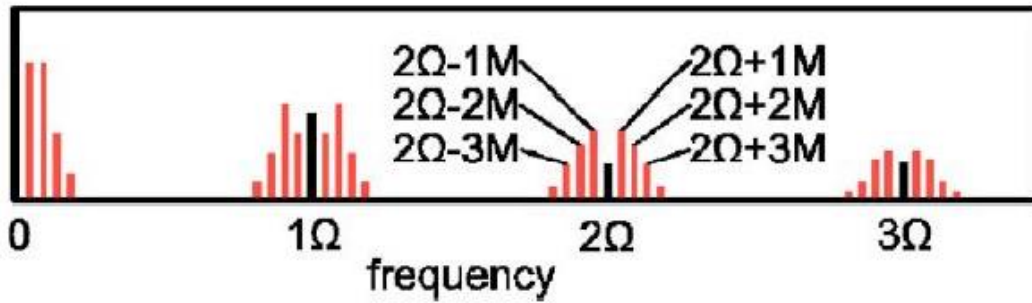


Figure 2.8 The oscillation of the reference mirror at frequency M in the pseudo-heterodyne detection [57]

Pseudo-heterodyne shows an intriguing and useful measurement detection setup. This detection method enables to measure the amplitude and phase of the near field in one measurement. It is also utilized for constantly changing homodyne detection. Besides these qualifications, some disadvantages exist for pseudo-heterodyne detection. First, it requires an expensive lock-in amplifier. Second, this measurement method is slightly complex and has a high tendency to create sources of noise by means of drift or mirror instability. Third, pseudo-heterodyne omits a big part of the actual signal falling on the detector more than a general lock-in a-SNOM. This situation occurs since each sideband of each tip harmonic peak transports

knowledge regarding the scattered near-field signal. However, only two of these sidebands can be observed in the pseudo-heterodyne detection. To sum up, the images caught by the pseudo-heterodyne detection have higher signal-to-noise ratios and less contrast in comparison with homodyne images [12].

2.4. Background Suppression with Using Higher Harmonic Demodulation

Separating the very small near-field signal from the huge background signal is the most significant point of detection of near-field signal. Higher harmonic demodulation detection can be utilized by all types of detection for separating pure near-field signal from the background signal. Since the near-field signal is very weak, we applied the interferometric detection to amplify the signal-to-noise ratio. However, the light scattered by the tip includes a contribution besides the desired enhanced near-field signal because of the reflections at the tip shaft as well as the far-field interferences in the experimental setup. Therefore, we utilize the method called higher harmonic demodulation [57].

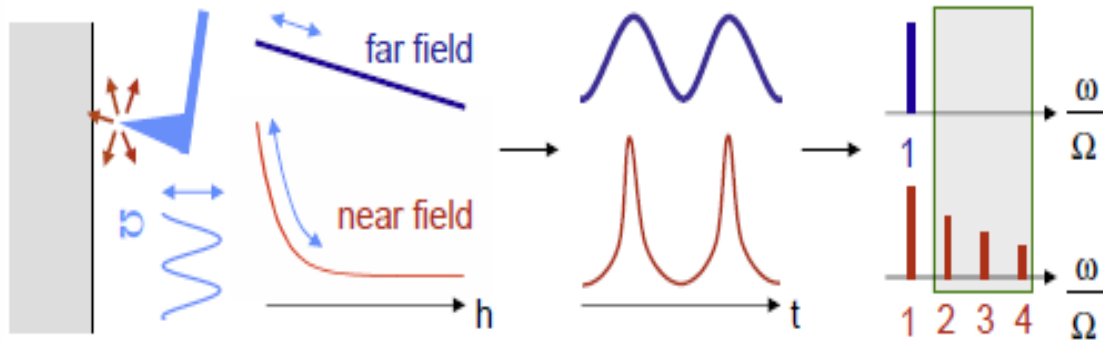


Figure 2.9 Basis of higher harmonic demodulation [58]

According to the in non-contact mode of AFM, the tip of a-SNOM oscillates at a certain frequency. Thus, the distance between the tip and the sample is modulated with the oscillation

frequency of the tip. Originally, the nonlinear distance dependence of a-SNOM system lead to a modulation not only in the tip frequency, but also higher harmonic frequencies. This nonlinear distance dependence suggests that with a sinusoidal modulation of the tip-sample distance, at frequency V , the scattering signal is obtained as an inharmonic modulation [30]. On the other hand, the far-field signal's background exhibits only a weak, essentially linear dependence on the distance between tip and sample. Therefore, the modulation of the background occurs only at tip oscillation's frequency. This feature enables to measure a pure near-field signal at higher harmonics using lock-in method as shown [56, 58].

CHAPTER 3

EXPERIMENTAL SETUP

3.1. The SR830 Lock-in Amplifier

Lock-in amplifiers utilize a method which is phase-sensitive detection to select the component of the certain reference frequency, because it compares AC electronic signals with the reference signal. Noise is eliminated by comparing these signals at frequencies other than the reference frequency signal. Thus, noise does not affect the measurement [59].

Using the lock-in amplifier is the most efficient method to track a signal at a set frequency. The tip oscillation frequency of a-SNOM system modulates the near-field optical signal. This reason makes sense only to these tip harmonics for achieving the desired signal without noise.

The lock-in amplifier used in our setup is a Stanford research SR830 lock-in. It has only one input that can be used as reference signals. We used it for detecting and measuring our small signal. Moreover, people are not able to realize near-field signal with naked eye, and we decided to develop a software for collecting data from the lock-in amplifier.

3.1.1. Software Development for Collecting Data from Lock-in Amplifier Remotely

3.1.1.1 VISA Communication VI

First, VISA communication VI is generated for performing the VISA communications as a write and read, as shown in figure 3.1. When we select the serial resource and the operations, Read, Write or both are performed. If both are selected, the VI will write the data first, then read the data, and then close the VISA session that is opened to the port.

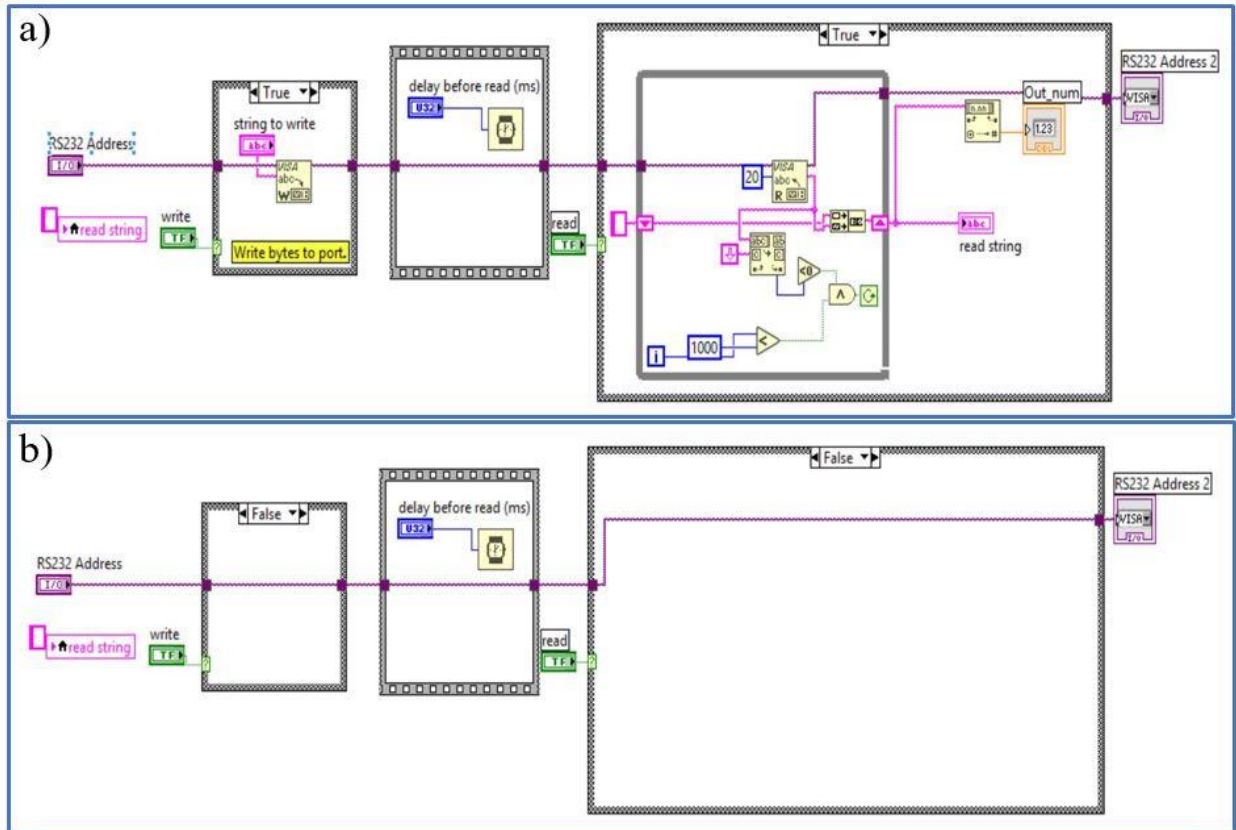


Figure 3.1. Block diagram of communication VI which a) works for write and read data b) does not work for write and read data

3.1.1.2. SubVIs for Specific Tasks

Several SubVIs are created for some specific tasks. The communication VI is used again. We created subVIs for different tasks to build communication tasks in the main program. The inputs are as commands, and the output is the reading response.

These SubVIs are Time Constant, Sensitivity, Source, Channel Display, Input Coupling, Harmonics, and File Property. The block diagram for all these SubVIs are shown below (Figure 3.2).

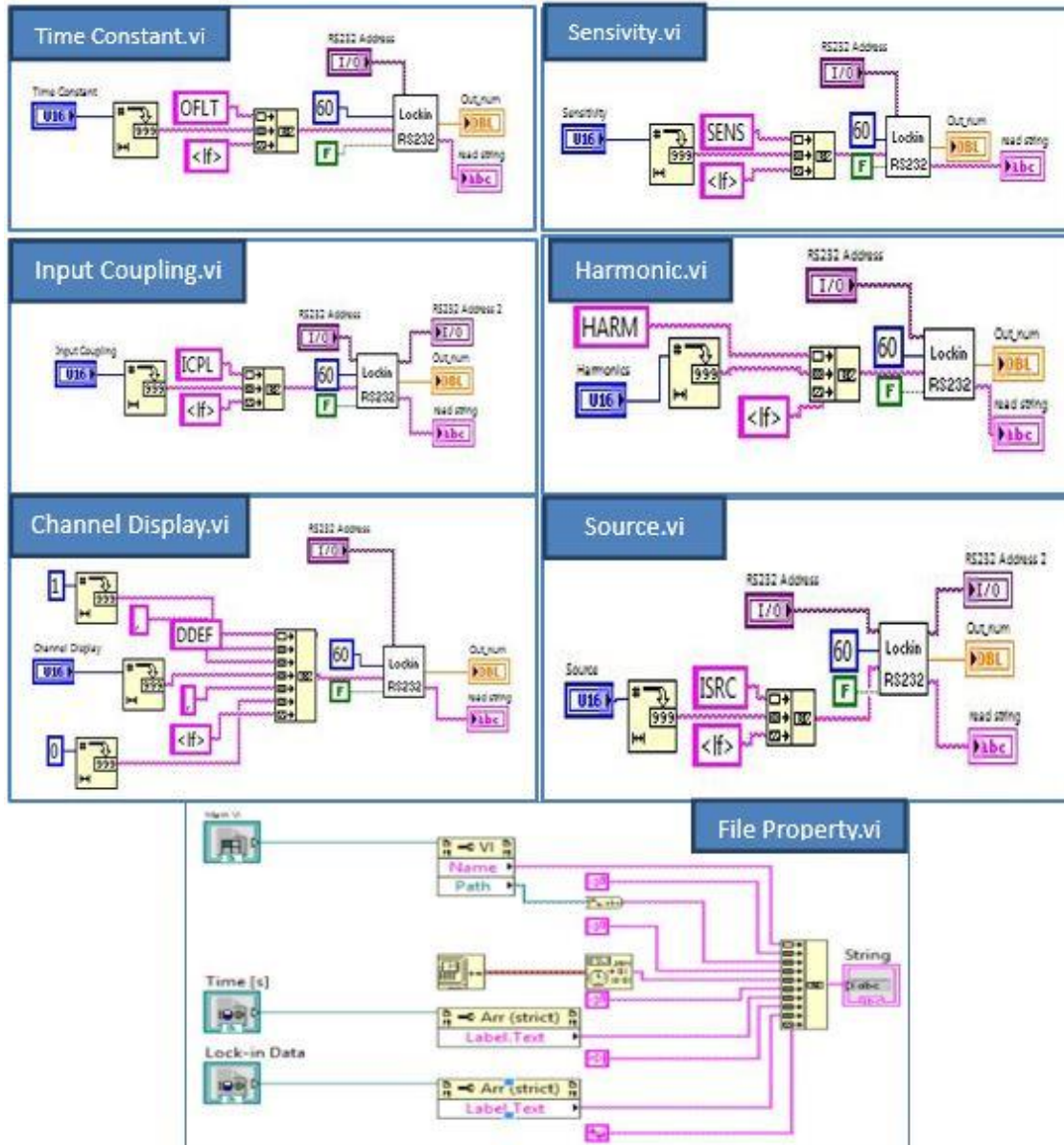


Figure 3.2 Block diagram of SubVIs for main program

All SubVIs have an input menu ring to let the users select different values for each setting. While the user changes the menu ring, the function command is sent to the SR830 Lock-in Amplifier.

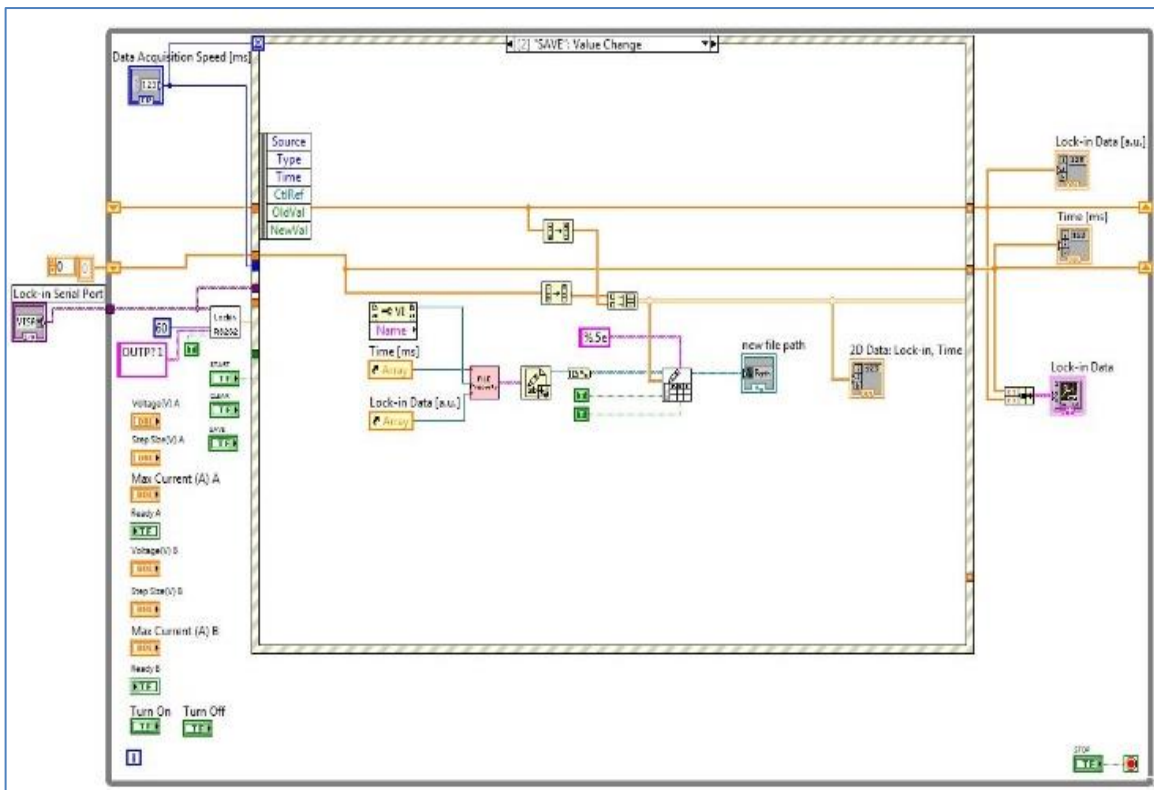


Figure 3.4 Block diagram of Save event

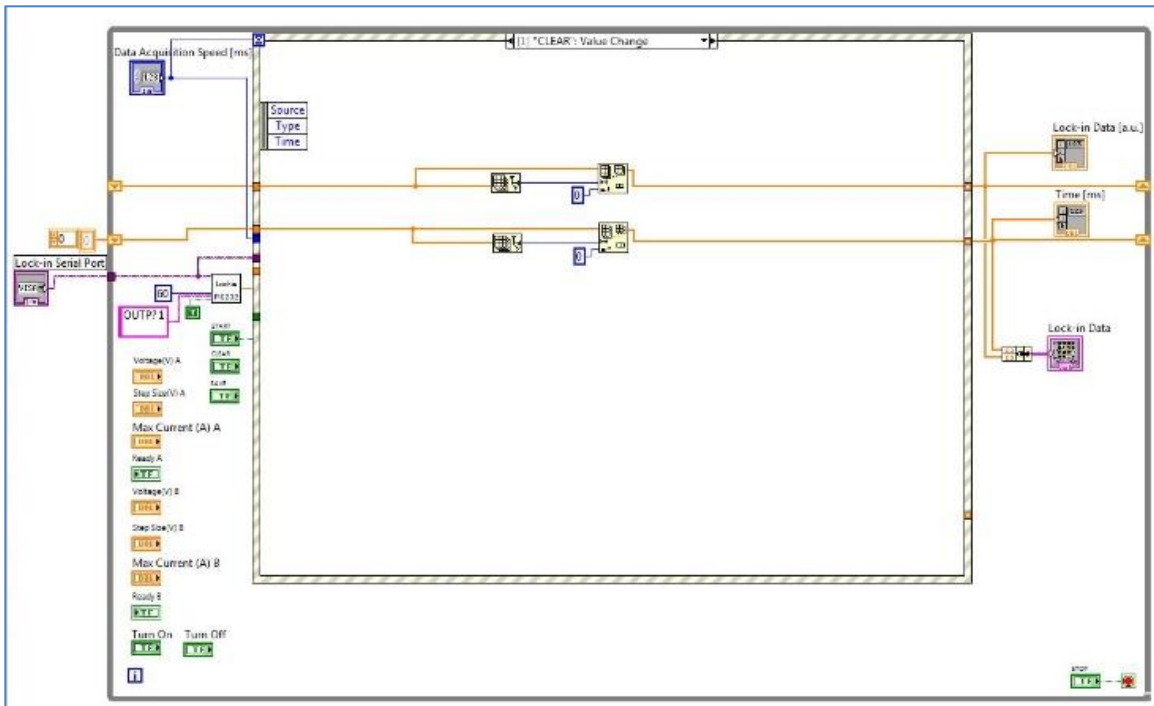


Figure 3.5 Block diagram of Clear event

In conclusion, after completing the code of program, we are able to collect all data and can make measurements fast. The final front panel design is shown in Figure 3.6.

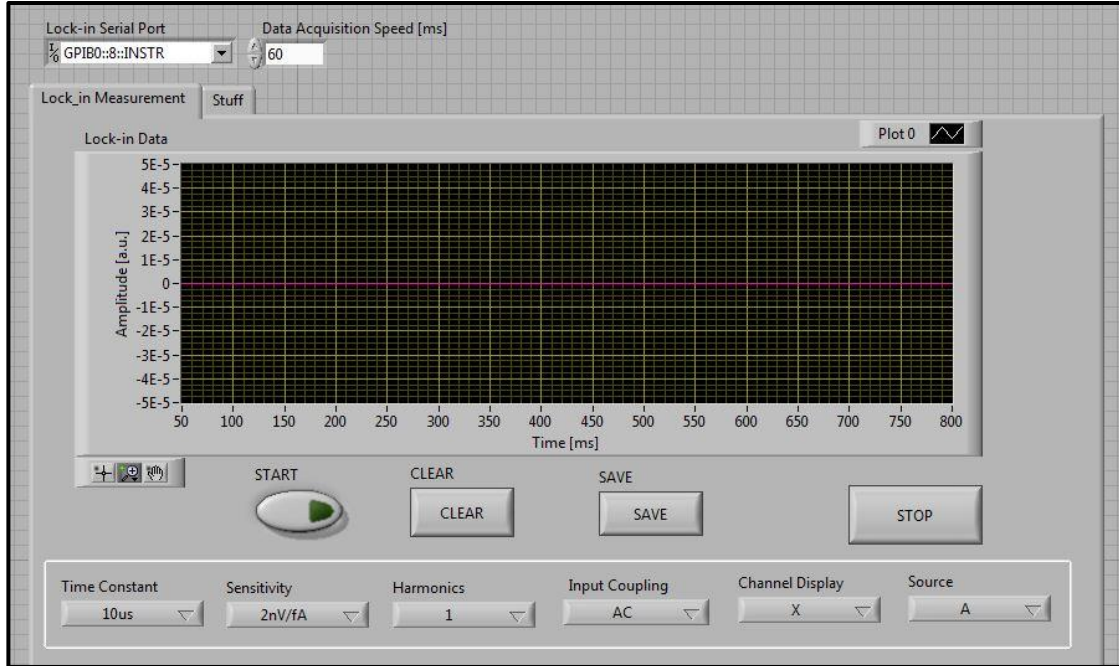


Figure 3.6 Front panel of main program

3.2. Parabolic Mirror

Incident light should be focused into a point where the apex of tip and sample interaction appear in the a-SNOM system. Scattering light from this area must go through the detector part after collection of the light scattered. It is easily noticed that the most useful way to focus and collect light is by using a parabolic mirror. In this way, enormous amounts of the small near-field scattered signal are obtained due to the parabolic mirror's giant numerical aperture [48]. This huge numerical aperture also enables to focus the incoming beam into a tight diffraction-limited spot. Moreover, the parabolic mirror helps in alignment. If the incident light is parallel to focal axis of the parabolic mirror, the light will always bend towards the focal point of the parabolic mirror. I used a parabolic mirror from Thorlabs which has a 4-inch long focal point.

3.3. Laser Source

We utilized a laser diode in the design of the a-SNOM system. The laser has wavelength of 520 nm, and its power is 50 mW. This laser diode is a compact light source that is suited for many kinds of applications, such as fluorescence and spectroscopic measurements, DNA sequencing, flow cytometry, imaging, and microscopy. Note that the laser diode shows different intensity within different temperatures as shown in the figure below.

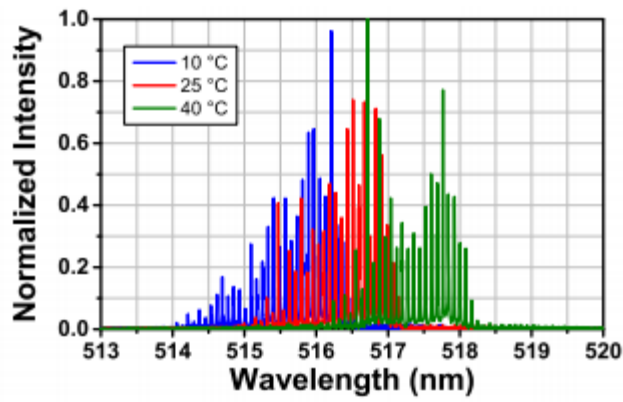


Figure 3.7 Output spectrum of laser diode

3.4. Photomultiplier Tube (PMT)

A photomultiplier transforms light into an electrical signal, and it boosts signal to a convenient level due to emission of secondary electrons. PMT consists of a photocathode, an electron-optical input system, an electron multiplier consisting of a series of secondary-emission electrodes, and an anode. The light flux transforms into the electron flux by a photocathode. Then, an anode gathers the electron flux from the multiplier and supplies the output signal [60].

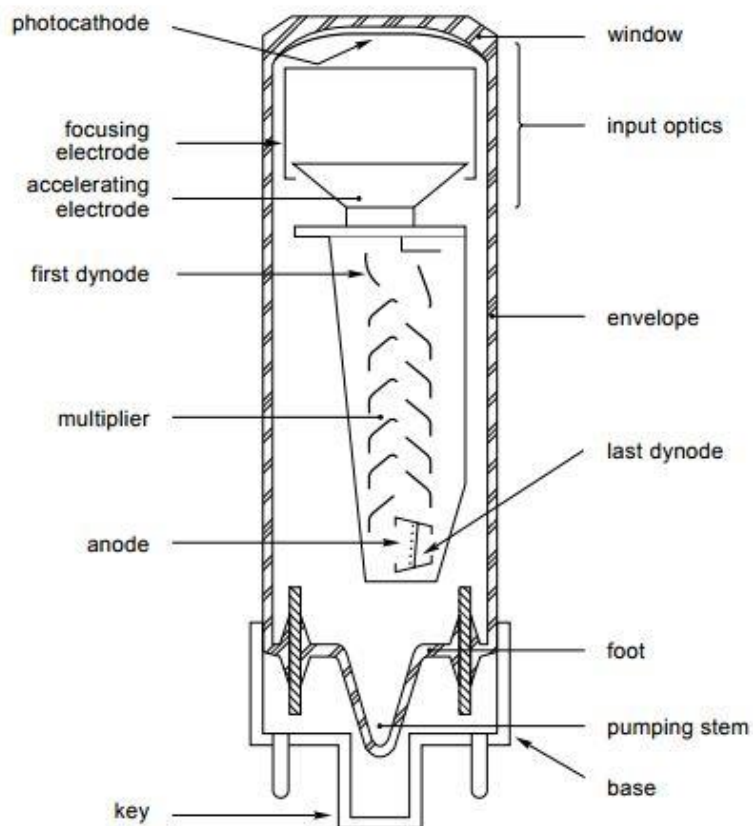


Figure 3.8 A photomultiplier's components [60]

Photoemission and second emission are fundamental phenomena for the photomultiplier's working principle. The electric field between dynodes accelerate and focus the electrons. For doing this, voltage supply provides the required potentials [60].

3.5 Nanopositioning System via MadPLL Controller

In order to measure the near-field signal, one needs to bring a probe into close proximity to a sample surface. Typically, the probe-sample distance is required to be in nanoscale to beat the diffraction limit and to reach the evanescent wave. As a result, most near-field microscopes use an automated feedback system that measures and maintains the appropriate probe-sample separation during measurement. Many near-field microscopes include a feedback system that maintains the probe sample separation by measuring shear forces with quartz tuning forks

[24,50]. The probe is attached to one of the tuning fork legs and extends beyond the edge of the leg, towards the sample. The tuning fork is driven at its resonance frequency and brought close to the surface [24]. When shear forces interact with the probe, the tuning fork's resonance frequency, amplitude, and phase will change [50]. The probe is brought towards the sample with the guidance of a controller. When an oscillation property of the tuning fork changes (e.g. resonance frequency, amplitude, or phase), the controller compares it to a predetermined set point. Therefore, the MadPLL-controlled nan positioning system is used to do that in the a-SNOM system.

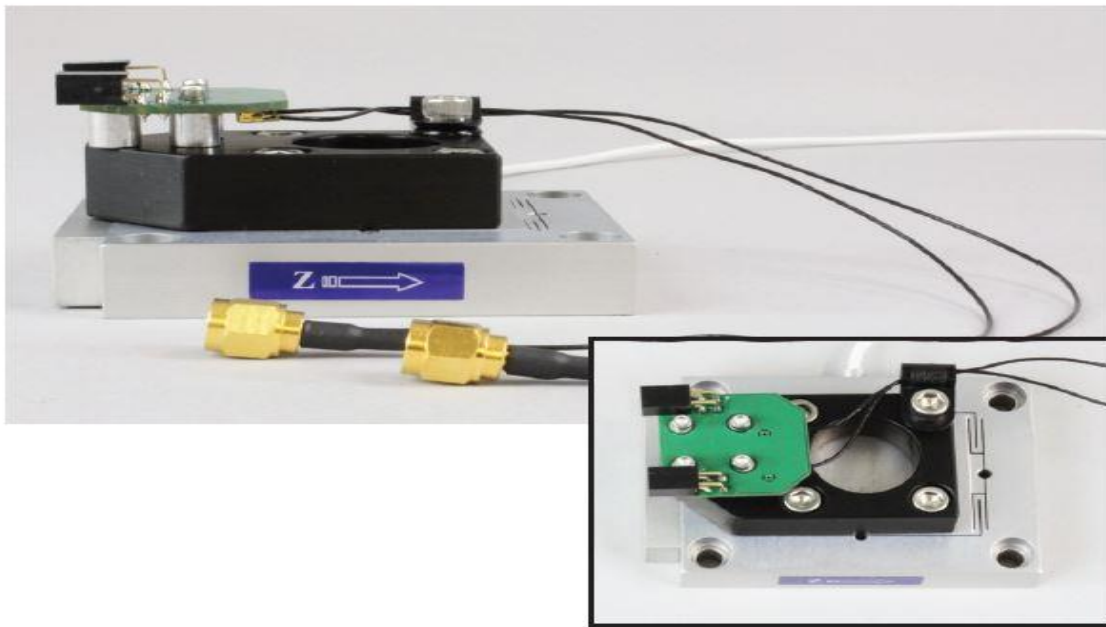


Figure 3.9 Nan positioning system

In our setup, MadPLL is a powerful instrument package that allows the user to create an inexpensive, high resolution resonant scan probe microscope. MadPLL has been specifically designed for resonant probes, such as tuning forks. In addition, it is fully compatible with Mad City Labs' high resolution nan positioning systems, which makes it easy for users to build a closed-loop scanning probe microscope with flexibility. Many of the functions of MadPLL are

fully automated and the included user-friendly MadPLL software allows complete control of user adjustable parameters. Among the software features are automated setup, configuration control, auto Q calculation and automatic parasitic capacitance compensation (PCC) control. These included features are designed to simplify setup and accelerate the data acquisition process. MadPLL is ideally suited for research and teaching laboratories, offering high performance, versatility, simplicity and excellent value.

Before using these components, the tip of the a-SNOM system should be attached with the tine of the tuning fork, and then the tuning fork should solder with the probe mount board of the nanopositioning system correctly for driving the probe within near-field signal range. We will explain how to prepare our setup step by step.

First, we have prepared near-field probes, a sharp tungsten tip made by electrochemical etching. Next, when we cut the tip to 2.5 mm long for reducing the mass of the tip on the tuning fork, we can achieve higher quality factor and performance of the system. Note that mounting a near-field tip is very important because a poor mount can reduce the tuning fork's quality factor and limit the system's performance.

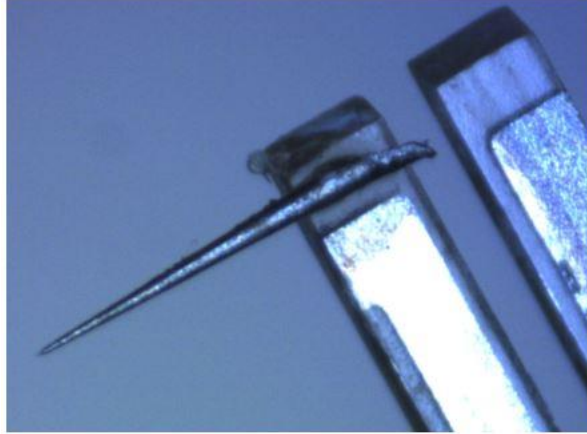


Figure 3.10 Optical microscope image of attaching tuning fork with tip (probe)

Secondly, after we have a 2.5 mm long-sharp tip, we need to mount this tip on the leg of tuning fork for using in the nanopositioning system. We apply super glue near the edge of the tuning fork tine, and we glue the tip with tuning fork. The amount of glue is also important to achieve high quality factor. We add glue on the tuning fork as little as possible during this process. Moreover, we glue the tip perpendicular to the tuning fork tine. Thus, the oscillation of the tuning fork tine will make the tip move towards and away from the sample surface.

Thirdly, we mount the tip on the tuning fork by using the probe mounting board, which is necessary for mounting the tuning fork on the nanopositioning system, as shown in figure 3.11.

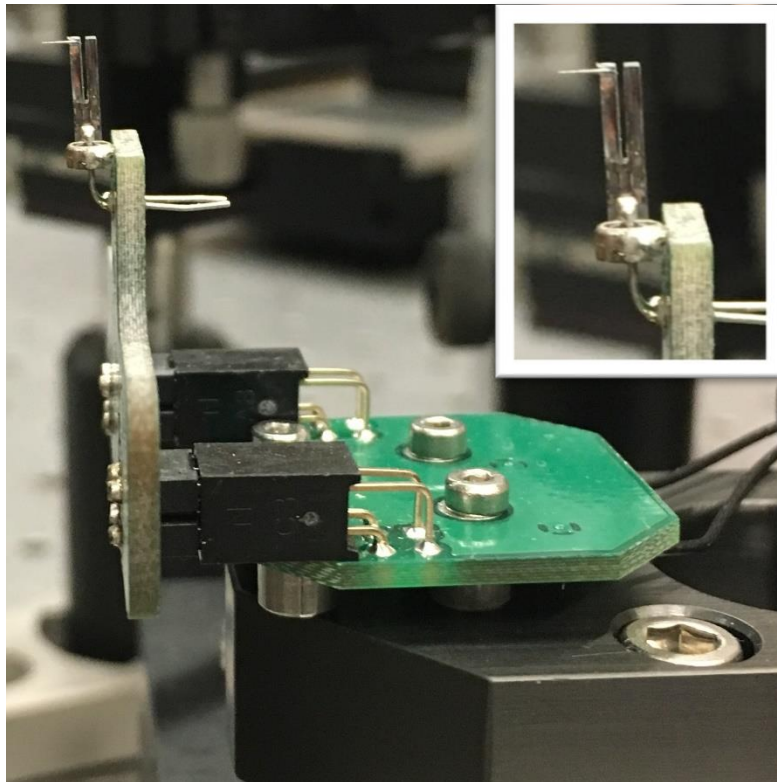


Figure 3.11 Tip of the tuning fork mounted on nanopositioning system

Then, we used the software of MadPLL to control the nanopositioning system, to keep the tip near the surface for achieving near-field signal. After calculating quality factor and oscillation frequency of the tuning fork, the nanopositioning system is ready to drive the tip near the sample surface within nanometers, with configuration adjustments made by the software of MadPLL.

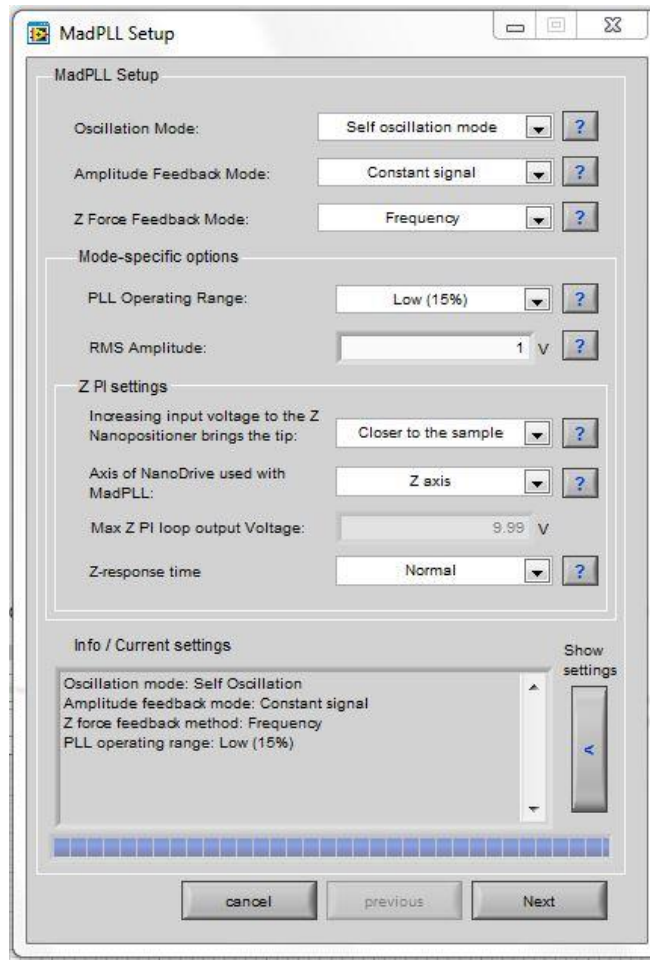


Figure 3.12 Setting variables picture of MadPLL software

Finally, when the configuration of nanopositioning system is completed, we brought the tip within 31 μm from the sample surface using a coarse positioner manually, because the range of the nanopositioning system is 31 μm . At the same time, we used optical microscope to avoid touching the sample surface and to protect the tip from bending the apex of it. Attaining tip-sample interaction for getting near-field signal, we are ready to use the approach process from MadPLL program. The nanopositioning system maintains the appropriate tip-sample separation during measurement.

3.6. Optical Alignment

Getting the near-field signal in a-SNOM measurement, one of the most important roles is to achieve the best optical alignment. Many reasons can affect the optical alignment: stability of mechanical setup, laser source, environmental factors, and so on. After eliminating these effects to a minimum, another important thing is that the incident light must be focused on the apex of the tip. The light scattered back from the tip is really weak and not uniform.

While aligning this laser beam on the tip's apex, I utilize irises to adjust the focal point of the laser on the sample-tip interaction. Moreover, I have a chance to see whether the light beam has the same height and goes straight through the whole path using irises. To focus the laser to the tip apex, the first thing is to be clear about the movements of the tip during the approach to the surface of the sample within the nanometer scale. Arranging this distance, I first used the coarse approach to bring the tip near the surface by hand under the optical microscope. After adjusting the tip within nanostage range, I have set up the control nanostage, which is at a range of 31 μm from the MadPLL controller. Thus, the tip oscillates at tuning fork frequency within nanometer scale close to the sample surface. When the focus spot of incident light is adjusted at the tip apex precisely, a shiny light appears between them. A sample retraction can be done to make sure there's enough separation between tip and sample. The laser spot should be very close to the tip now. It is checked by the optical microscope. After the laser spot is aligned to the tip apex, the approaching process can be conducted. The feedback loop will engage to maintain the tip-sample distance. Hereby, we reach the near-field signal.

CHAPTER 4

RESULTS

The goal of my study is to build a practical a-SNOM system using SPM technique. We used self-homodyne detection among the interferometric detection. Figure 4.1 shows the detection schema of my a-SNOM setup. Besides, the real optic setup photo is shown in Figure 4.2.

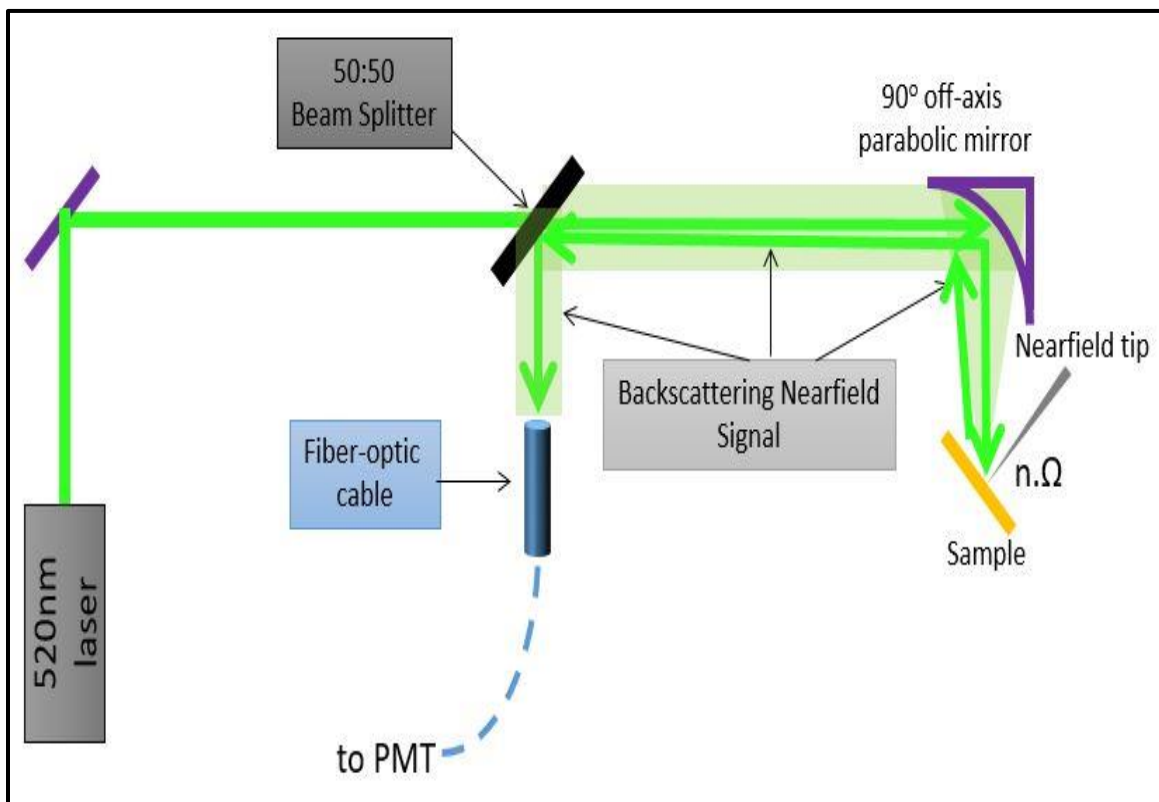


Figure 4.1 Schematic diagram of our self-homodyne detection setup

Bringing the tip within nanoscale separation between the etched tungsten tip and the surface of copper sample is carried out using MadPLL controlled nanopositioning system. Thus, the near-field signal phenomenon is achieved. Two different tungsten tips are obtained by using electrochemical etching technique to detect near-field signal.



Figure 4.2 Photo of our optical setup

4.1. Preparing the Near-Field Tip by Electrochemical Etching Result

A metal etching process involves an electrolyte solution, an anode and a cathode. The electrochemical etching idea is based on immersion of a small diameter metal wire into an electrolyte solution where there is an opposite electrode in the solution. Then, AC or DC voltage

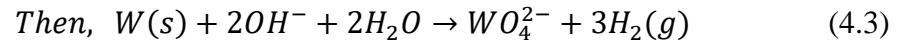
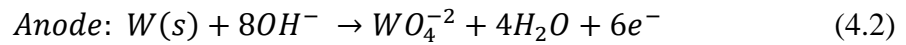
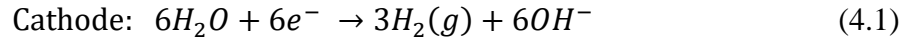
is applied between these two electrodes. When enough dissolution of the wire is achieved, it shows a sharp tip shape. Every material for obtaining the tip has its own choice of the electrolyte solution and the voltage value to be applied [61,62].

The most common electrolytes used for tungsten (W) etching are NaOH and KOH [63]. We used a 5 M / 200 mL KOH solution. Figure 4.3 shows how to connect the tungsten tip and steel rod and our electrochemical etching process setup.



Figure 4.3 Photo of our electrochemical etching setup

When a positive voltage is applied to the dead tungsten tip, etching starts in the air and the electrolyte solution interface. The following overall electrochemical reaction happens, while we are obtaining the near-field tip [63].



After applying this process to obtain our near-field tip, we have approximately 5 μm and 1 μm sharp apex of tips respectively, as shown Figure 4.4 and Figure 4.5.

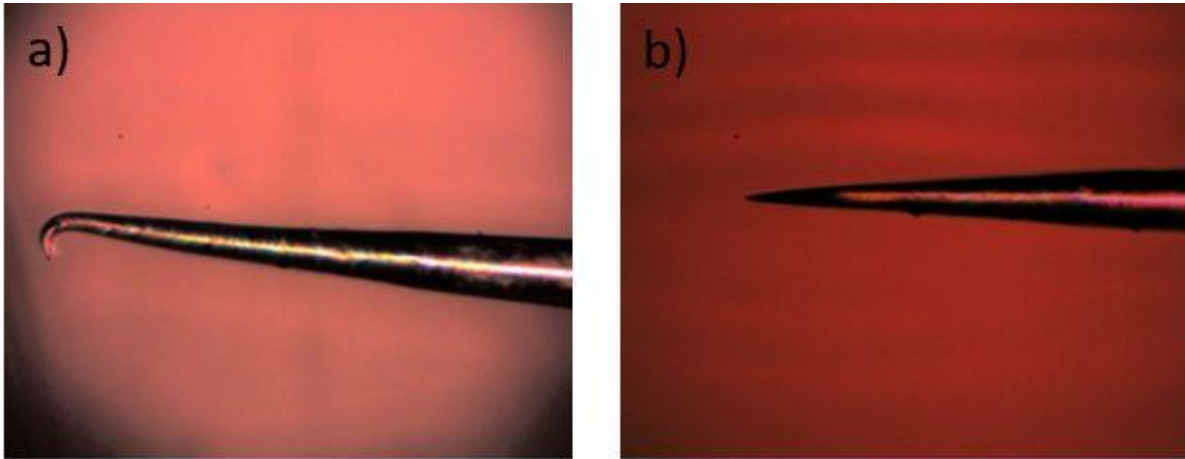


Figure 4.4 Optical microscope images of first tungsten tip a) before electrochemical etching process b) after electrochemical etching process

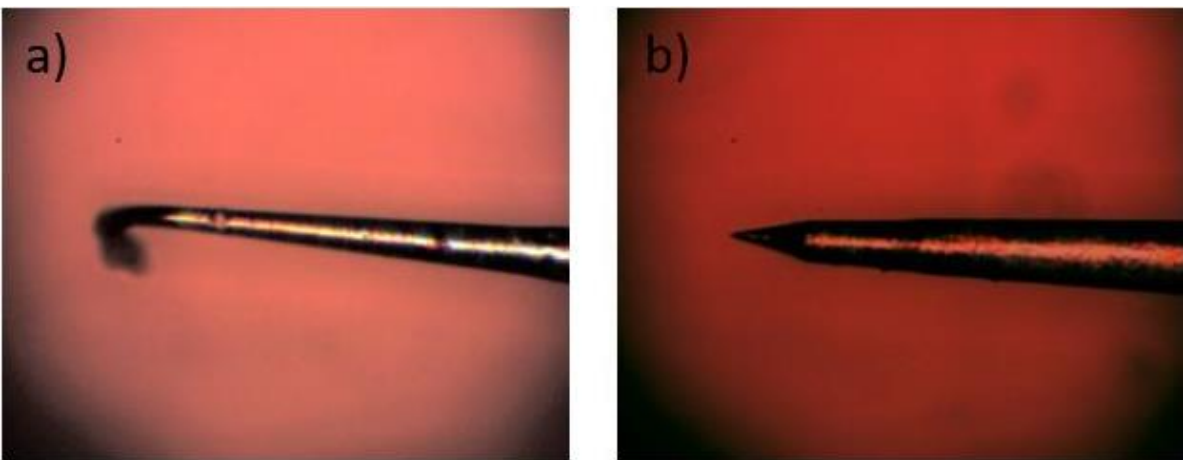


Figure 4.5 Optical microscope images of second tungsten tip a) before electrochemical etching process b) after electrochemical etching process

After getting the first tungsten tip, which has approximately 4–5 μm tip apex diameter, we applied 3 V, reaching 3.2 mA current. On the other hand, to the second tungsten tip which has approximately 1 μm tip apex diameter, 3V is applied, reaching 0.2mA current.

4.2. Near-Field Generation and Detection Using Two Different Tungsten Tips

With the first tungsten tip, we detected the first, second and third harmonic of the near-field signal based on amplifying the near-field signal and the suppression background signal theories, which are mentioned in the second chapter, with the lock-in detection technique.

First, the oscillation frequency and quality factor of the tuning fork is calculated by the MadPLL software for the first tungsten tip, which is obtained by electrochemical etching. The first tip profile is shown in the Figure 4.6.

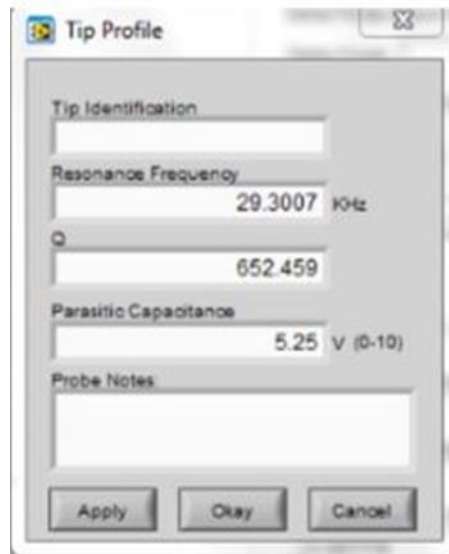


Figure 4.6 Tip profile of first etched tip (app. 4–5 μm)

When separation of the sample surface and tip is in the nanoscale or the tip is engaged with the sample surface, the near-field signal is measured. If the tip is not engaged with the sample surface, we are not able to measure the near-field signal. The near-field signal is measured up to the third harmonic of reference frequency clearly. The following graphs are

plotted by collecting data with the LabVIEW program at first, second and third harmonic of the reference frequency simultaneously.

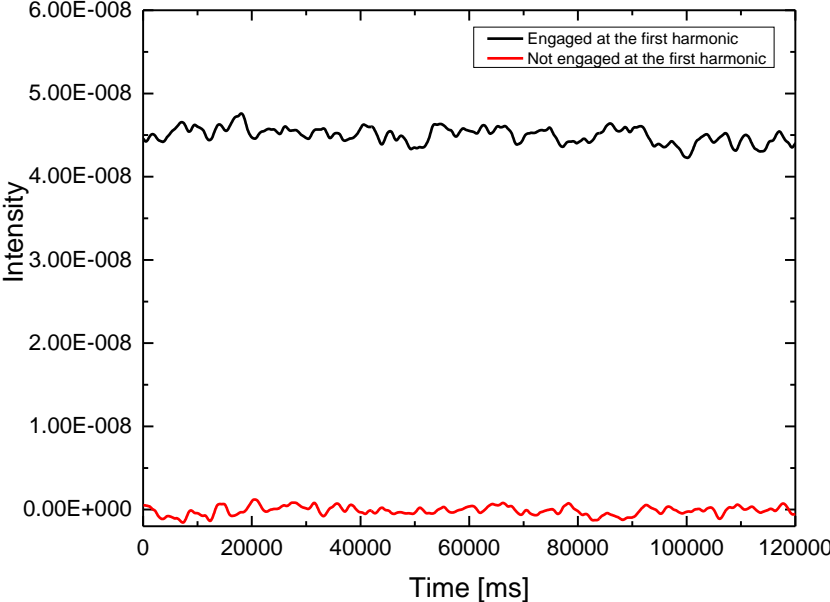


Figure 4.7 Graph of near-field signal with first etched tip at first harmonic

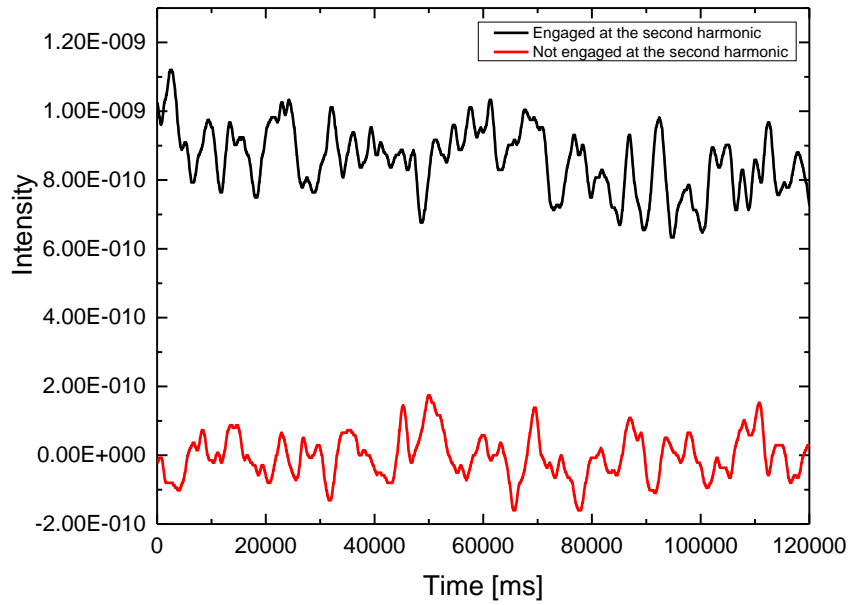


Figure 4.8 Graph of near-field signal with first etched tip at second harmonic

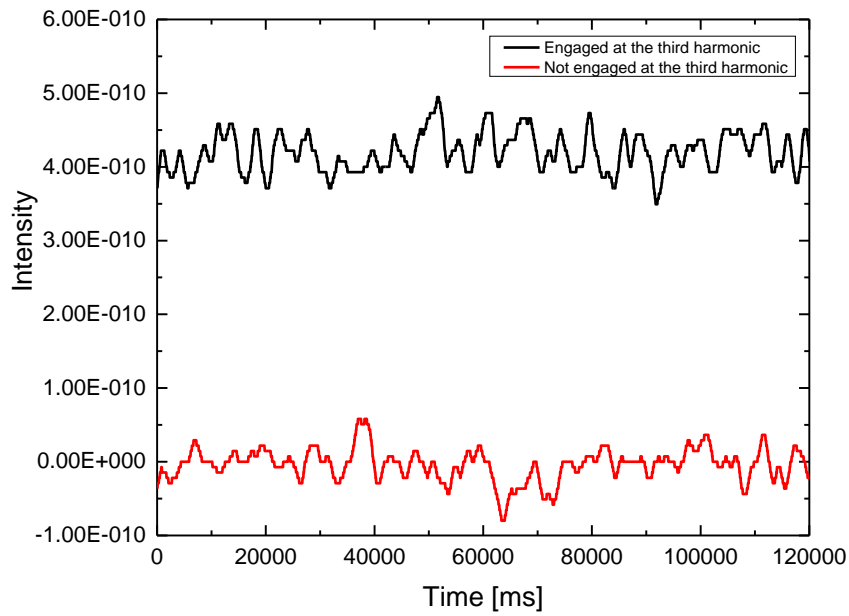


Figure 4.9 Graph of near-field signal with first etched tip at third harmonic

Figure 4.10 shows the comparison of all the three harmonic detections of the near-field signal in one graph.

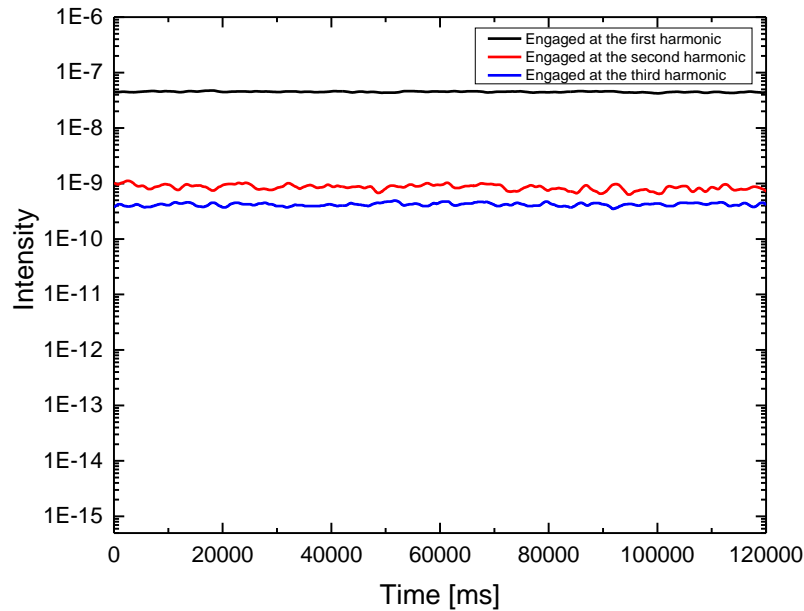


Figure 4.10 Graph of the detected harmonic of near-field signals where all are together

After achieving this result with 4–5 μm thick apex of tip, we changed the tip on the tuning fork with the second tungsten tip which has approximately 1 μm sharp apex diameter in order to introduce resolution of our signal. After attaching this tip in our measurement setup, MadPLL calculated the oscillation frequency and quality factor again. The following figure shows these values.

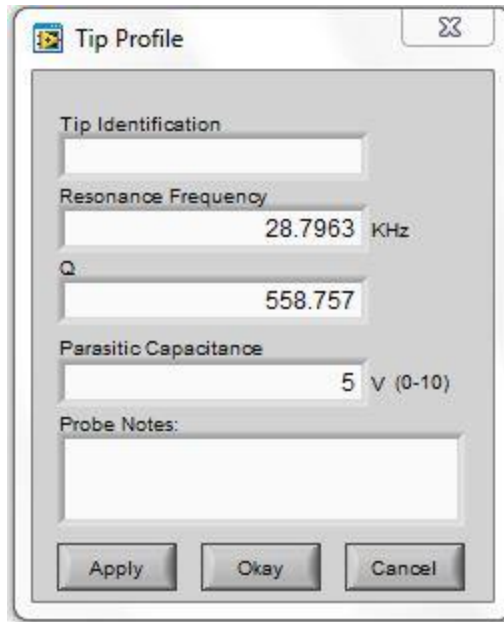


Figure 4.11 Tip profile of second etched tip (app. 1 μm)

Same procedure is followed like the first tip result. However, the near-field signal is measured up to the second harmonic of reference frequency clearly. The third harmonic signal is not separated from the background because of low signal-to-noise ratio. All results are shown in the following graphs.

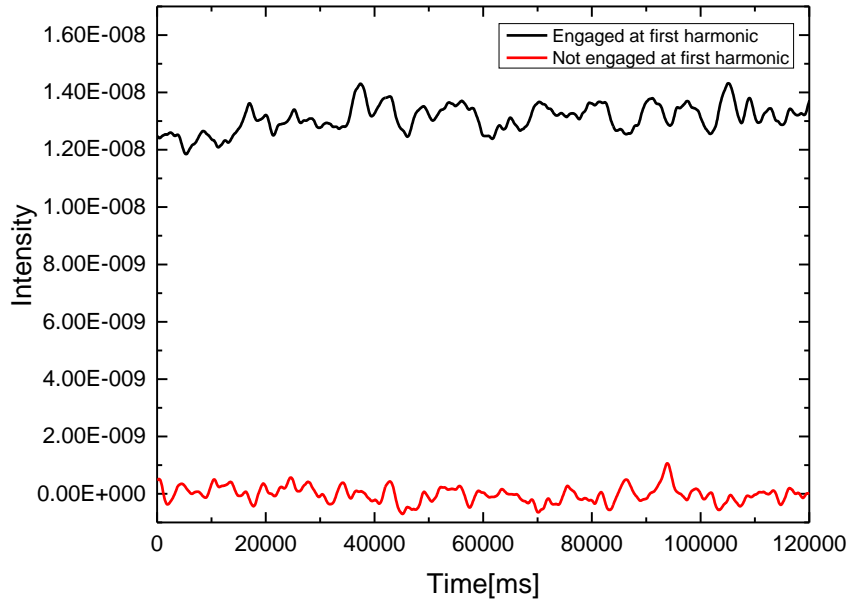


Figure 4.12 Graph of near-field signal with second etched tip at first harmonic

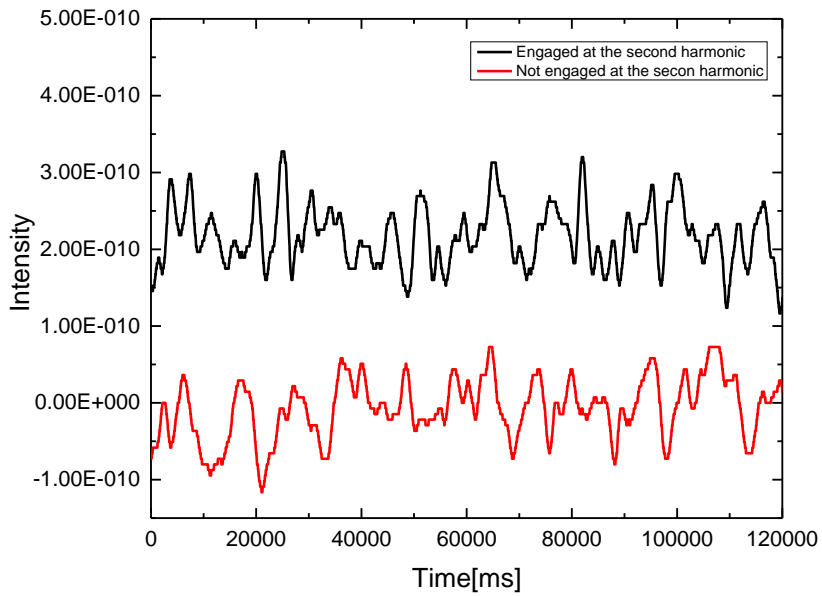


Figure 4.13 Graph of near-field signal with second etched tip at second harmonic

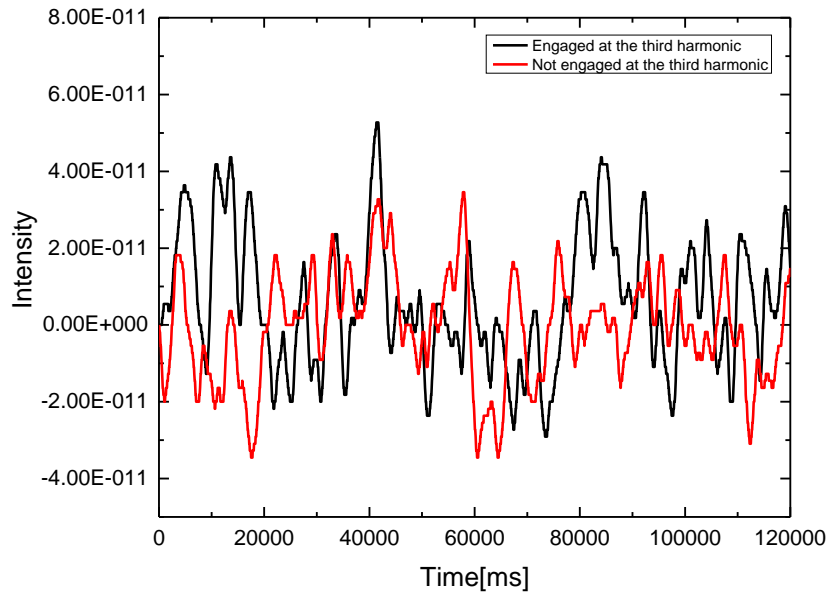


Figure 4.14 Graph of near-field signal with second etched tip at third harmonic

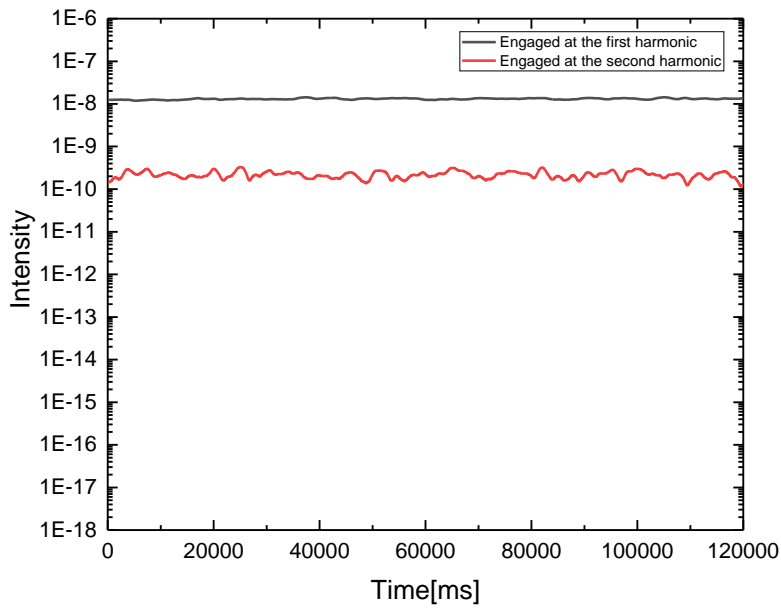


Figure 4.15 Graph of the detected harmonic of near-field signals where both are together

When the first and second harmonic near-field signal intensity is compared for both tips, it is seen that the signal intensity is dropped as expected, as shown in Figure 4.15. However, the quality of near-field signal at the second harmonic is higher than at the first harmonic based on the background suppression at the higher harmonic. Other group research is verified by obtaining the near-field image of Au electrode on LAO/STO using 10.2 μm wavelength in the pseudo-heterodyne method, as shown in Figure 4.16.

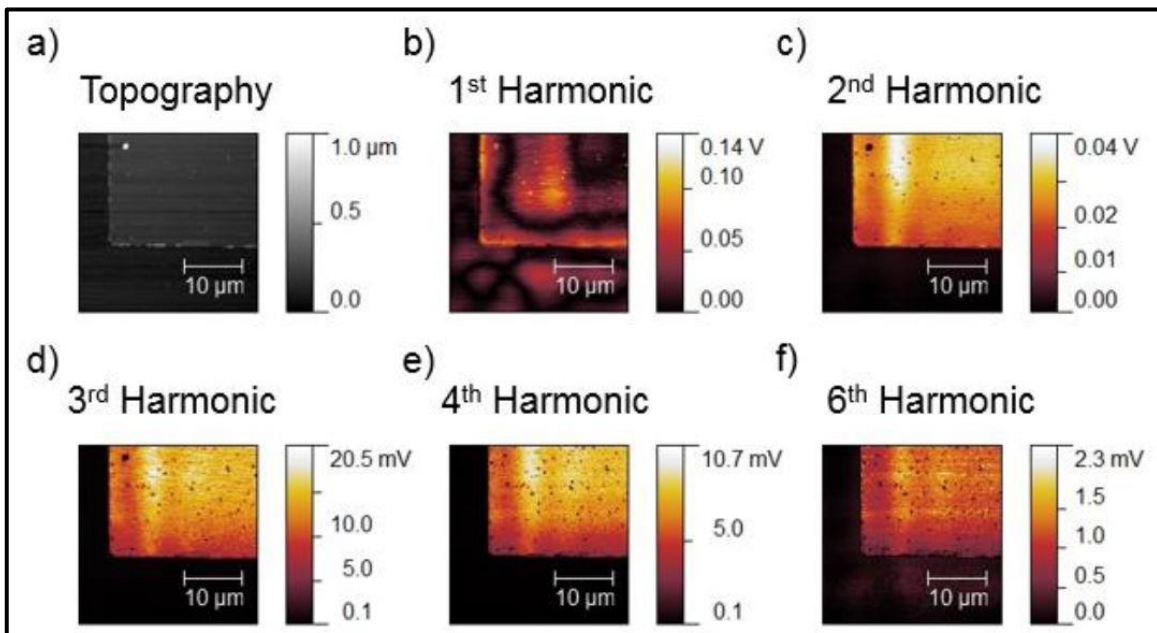


Figure 4.16 Different demodulation harmonics of near-field amplitude images using Au electrode on LAO/STO as a sample of pseudo-heterodyne detection [64]

The first harmonic demodulation shows a contrast in areas consisting of a constant material because of background signal effects. The second and higher harmonics of near-field images represent clearance due to the suppression of background signal effect. However, demodulation at higher harmonic does not mean getting rid of the whole background signal effect. On the other hand, when the a-SNOM system reaches the higher harmonics, such as the 6th harmonic which is obtained by other research groups, the image is represented to be noisy

because of a low signal-to-noise ratio. It shows that there is a limitation about using demodulation at the higher harmonic [64].

4.3. Near-Field Signal Enhanced Photoluminescence of MoS₂ Result

Recently, layered transition metal dichalcogenides (TMDCs) have received great interest due to their interesting physical properties and potential applications in optoelectronics. One of the most studied and widely used layered transition metal dichalcogenide (LTMD) has been molybdenum disulfide (MoS₂). It has unique electrical, optical, chemical and mechanical properties, which makes it striking to use as a hydrodesulphurization catalyst [65, 66]. Moreover, it behaves as active materials or transport material in solar cells [67], as photocatalysts [68], as electrodes in lithium batteries [69], and as a solid lubricant [70].

Optical transitions in MoS₂ can be probed using absorption or photoluminescence (PL) spectroscopies. The PL in bilayer and bulk MoS₂ is significantly lower compared to monolayer samples as there is a crossover from indirect to direct band gap material [71]. This crossover from direct-indirect band gap produces large disparity in the quantum efficiency between bilayer and monolayer MoS₂. Photoluminescence in MoS₂ can be a perfect test for noticing the indirect to direct band gap conversion from bulk to single layer.

Therefore, molybdenum disulfide sample on sapphire substrate is used in this measurement. With the a-SNOM system, the surface waves in the visible range are excited by 520 nm laser source on the MoS₂ sample. Due to these reasons, a-SNOM system is used in order to observe field enhancement of MoS₂. We achieved enhancement result of photoluminescence of MoS₂ on sapphire substrate at 2 kHz reference frequency of the tip. When the tip is engaged, we can realize that there are enhanced peaks around 634 nm; besides, the tip is not engaged, as shown in the figure.

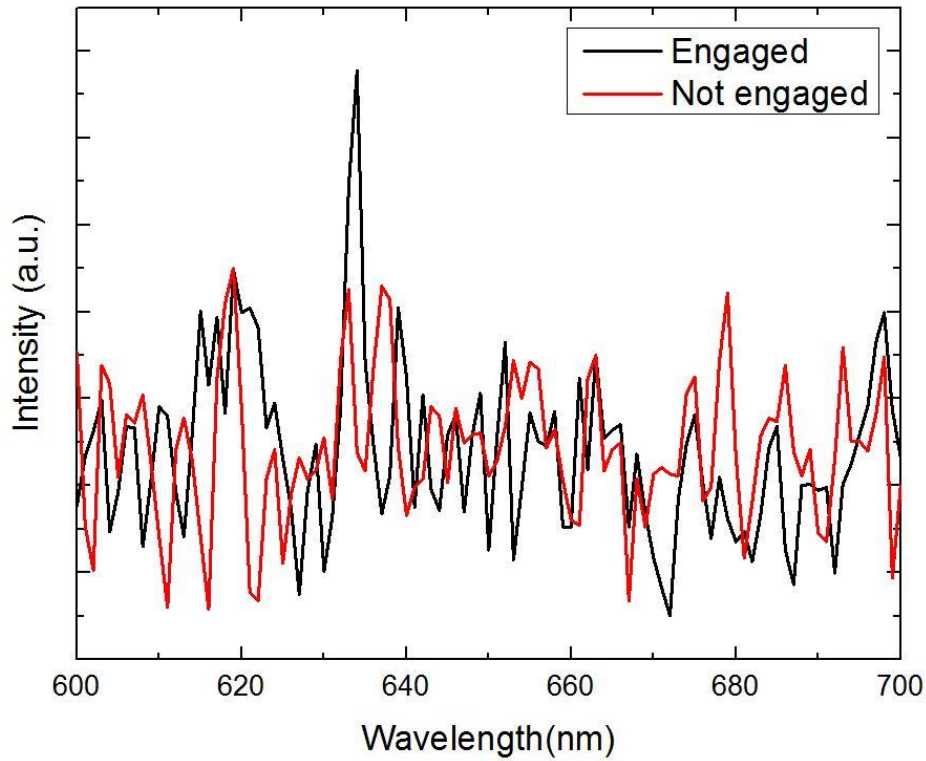


Figure 4.17 Graph of measuring MoS₂ with a-SNOM setup

CHAPTER 5

FUTURE WORK AND CONCLUSION

5.1. THz-Time Domain Spectroscopy (THz-TDS)

The THz-time domain spectroscopy is a very accomplished and highly used technique using THz waves to characterize materials based on its unique responses in the THz region. By utilizing electromagnetic pulses with sub-picosecond width, the THz-TDS has obtained sample properties in the THz frequency regime, which is between 0.2 and 2 THz for our setup. The THz-TDS setup is composed of multiple optical mirrors, a beam splitter, delay stage, an emitter part and a detector part. The THz pulse is generated in the emitter part and sensed in the detector part. Based on sample interest, it has reflection and transmission mode geometry. The femtosecond laser input pulses at a wavelength of 790 nm with a repetition rate of 76 MHz is supplied by a mode-locked Ti:Sapphire ultrafast laser. Then, the laser beam reaches a polarized beam splitter (BS). This BS splits the laser beam into a pump beam and a probe beam. The pump beam energy is much higher than the probe beam energy because the pump beam generates the THz pulses. The half-wave plate can adjust the ratio of these two beams just before the BS. When the pump beam goes to the emitter module of THz-TDS, it is adjusted to focus on the gap of photoconductive antenna (PCA). This gap is around 50 μm . Thus, a 90° off-axis parabolic mirror collimates the emitted THz pulse. At the same time, after the probe beam passes a mechanical delay line, which makes time delay between the pump and probe beams, it reaches the receiver module of THz-TDS. In order to focus the THz wave radiation onto the sample and re-collimate

it after it is transmitted through the sample, two polyethylene (PE) lenses are used. And then, the transmitted THz pulse and the probe beam interact in the receiver module.

The probe beam interacts with the electric field of incoming THz pulse. The delay stage changes the timing of gating laser pulse and controls this interaction. Thus, the amplitude of the electric field of THz pulse as a function of time is measured. The detector's output is usually followed by a lock-in amplifier increasing the signal-to-noise ratio (SNR). Many THz-TDS setups utilize DC bias for PCA emitter, and utilize mechanical chopper to modulate the pump beam as a reference frequency for detection. However, our PCA emitter is biased with a square wave, and its frequency (15 kHz) is used as a reference frequency for the lock-in process in our setup.

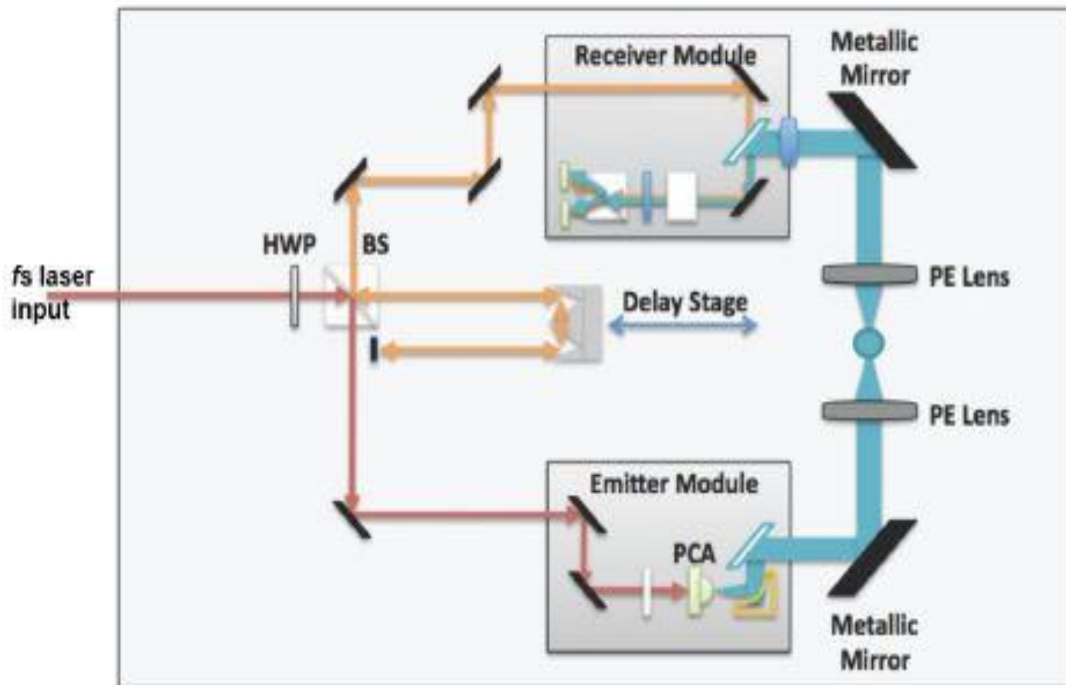


Figure 5.1 THz-time domain spectroscopy schema. The sample is measured in the middle of the two PE lenses [73]

5.2 Integration of Near-Field System on THz-TDS

For future research, we want to move the near-field signal detection setup to the THz-TDS system. We used the self-homodyne detection to amplify the near-field signal in this thesis and the reflection mode for detecting the near-field signal. When we move to a-SNOM setup on the THz-TDS system, we will face some difficulties. The first reason is that the emitter beam path and the THz wave path should be equal to the probe beam path. The other reason is the position of the detector part in the near-field signal detection setup: It causes an obstacle for the THz-TDS system.

In order to handle the first obstacle, we can use two parabolic mirrors (60° is preferable) – one to focus THz on the sample, the other to re-collimate the THz wave. Figure 5.1 uses a third parabolic mirror (90° is preferable) to focus onto the PCA detector. Using the PCA requires a probe laser beam to be focused onto the antenna gap. This probe beam can be carried by three extra flat mirrors, as seen in Figure 5.1. We will carefully estimate the distances and see whether the emitter beam path and the THz wave path are equal to the probe beam path. If the difference in the distances cannot be compensated by the delay stage (i.e. probe beam path may turn out to be longer), then we can propose the scheme in Figure 5.2 where the third parabolic mirror is omitted. The second parabolic mirror is readjusted to translate the THz wave in the reverse direction. In this case, PCA is replaced closer to the main board of THz-TDS. In this scheme, since the third parabolic mirror is omitted, the THz wave going into the PCA detector is not focused, but collimated. Moreover, the detection part of the near-field signal at THz-TDS is moved to close the tip-sample interaction in both figures for getting rid of the other reason.

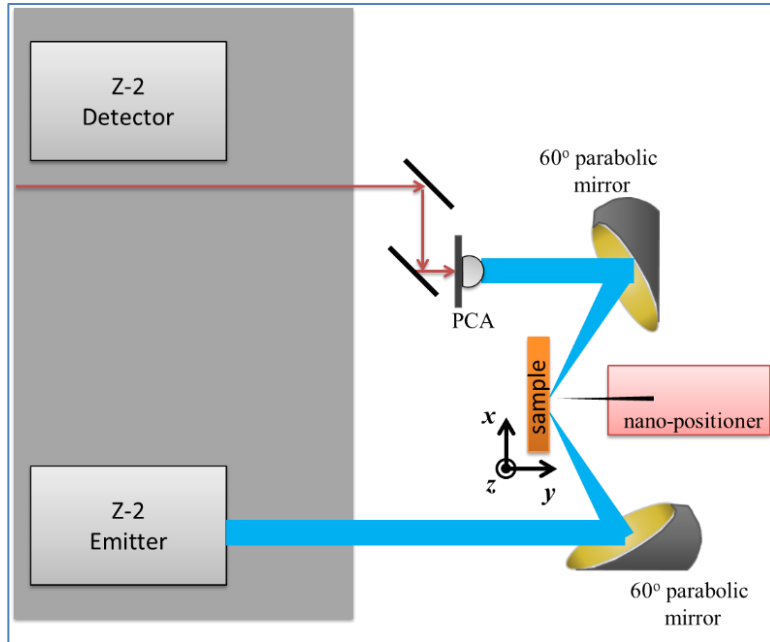


Figure 5.2 Schematic diagram of small probe beam path near-field detection setup in THz-TDS

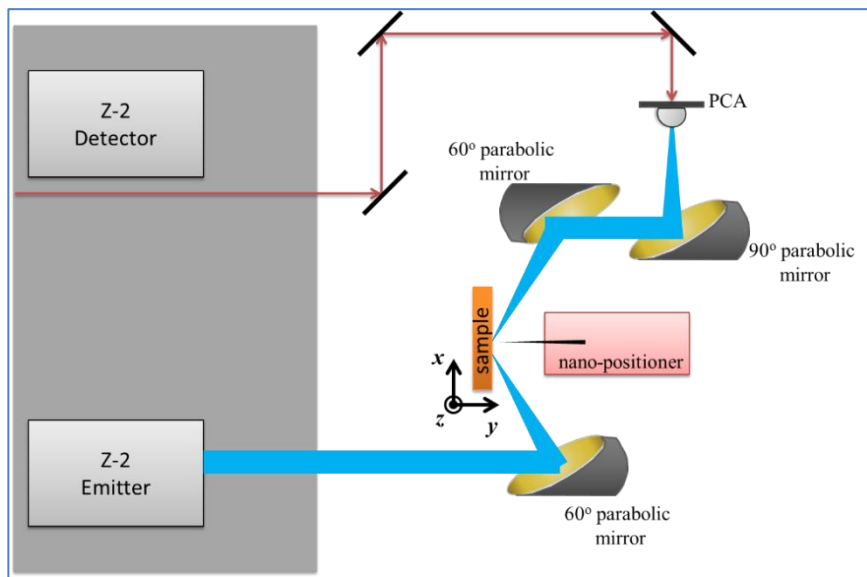


Figure 5.3 Schematic diagram of long probe beam path near-field detection setup in THz-TDS

5.3 Conclusion

This thesis organized the practical design of scattering type-scanning near field optical microscope. The idea is that the system focuses light on the sample surface and apex of tip. It detects the reflected light from tip-sample interaction, which contains information about the material, using the interferometric setup. Before achieving the near-field signal in this thesis, the sharp tips are produced by using the electrochemical etching process. Approximately, 1 μm and 5 μm diameter of tip apex are demonstrated. Then, it is attached to the tuning fork. Another component of the setup is the nanopositioning system. It is investigated to maintain the distance between the sample surface and tip within nanoscale. Producing the sharp tip, setting interferometric detection up, and using the nanopositioning system, we have achieved the near-field signal phenomena. In addition to achieving pure near-field signal as much as possible, the higher demodulation lock-in technique is utilized.

Importantly, when a-SNOM is used as a measurement technique, researchers are able to measure potentially nanoscale structures in their own samples in many different areas. The resolution signal is only based on apex of tip diameter instead of diffraction limit.

REFERENCES

- [1] Y. Li, “Investigation of optical near field using near field scanning optical microscopy,” 2014.
- [2] Anon. (2017). [*Big Things from a Tiny World*] Available: https://www.nano.gov/sites/default/files/pub_resource/nanotechnology_bigthingsfromatinyworld-print.pdf
- [3] L. Pauling, “Metal-metal bond lengths in complexes of transition metals,” *Proc. Natl. Acad. Sci.*, vol. 73, no. 12, 1976, pp. 4290–4293.
- [4] S. A. Centeno, F. Schulte, N. W. Kennedy, and A. G. Schrott, “The formation of chlorine-induced alterations in daguerreotype image particles: A high resolution SEM-EDS study,” *Appl. Phys. A Mater. Sci. Process.*, vol. 105, no. 1, 2011, pp. 55–63.
- [5] W. Clauss, D. J. Bergeron, and A. T. Johnson, “Atomic resolution STM imaging of a twisted single-wall carbon nanotube,” *Phys. Rev. B*, vol. 58, no. 8, 1998, p. 4.
- [6] G. Binnig, C. Gerber, E. Stoll, T. R. Albrecht, and C. F. Quate, “Atomic resolution with atomic force microscope,” *EPL (Europhysics Letters)*, vol. 3, no. 12, 1987, p. 1281.
- [7] I. Lisiecki, A. Filankembo, H. Sack-Kongehl, K. Weiss, M.-P. Pileni, and J. Urban, “Structural investigations of copper nanorods by high-resolution TEM,” *Phys. Rev. B*, vol. 61, no. 7, 2000, pp. 4968–4974.
- [8] P. L. Stewart, S. D. Fuller, and R. M. Burnett, “Difference imaging of Adenovirus: Bridging the resolution gap between X-ray crystallography and electron microscopy,” *EMBO J.*, vol. 12, no. 7, 1993, pp. 2589–2599.
- [9] C. Bai, *Scanning Tunneling Microscopy and its Applications*. New York, NY: Springer Verlag, 2000.
- [10] A. Marian, M. C. Stowe, J. R. Lawall, D. Felinto, and J. Ye, *Science*. New York, NY, 2004, pp. 306, 2063.
- [11] G. Saxby, *The Science of Imaging*. CRC Press, 2002.

- [12] J. A. Gerber, “Real-Time Detection for Scattering Scanning Near-Field Optical Microscopy,” 2013.
- [13] G. R. Fowles, *Introduction to Modern Optics*, vol. 36, no. 8. 1968.
- [14] F. L. Pedrotti and L.S. Pedrotti, *Introduction to Optics*. New Jersey: Prentice Hall, 1987.
- [15] E. C. Kinzel, “Ridge Aperture of Optical Antennas,” 2010.
- [16] D. V. Kazantsev, E. V. Kuznetsov, S. V. Timofeev, A. V. Shelaev, and E. A. Kazantseva, “Apertureless near-field optical microscopy,” *Physics-Uspekhi*, vol. 60, no. 3, 2017, pp. 259–275.
- [17] S. Salapaka and M. Salapaka, “Scanning Probe Microscopy,” *IEEE Control Syst. Mag.*, vol. 28, no. 2, 2008, pp. 65–83.
- [18] R. Wiesendanger, *Scanning Probe Microscopy and Spectroscopy: Methods and Applications*. Cambridge University Press, 1994.
- [19] P. Vettiger, G. Cross, M. Despont, U. Drechsler, U. Durig, B. Gotsmann, W. Haberle, M. A. Lantz, H. E. Rothuizen, R. Stutz, and G. K. Binnig, “The ‘Millipede’ - Nanotechnology Entering Data Storage,” *IEEE Trans. Nanotechnol.*, vol. 1, no. 1, 2002, pp. 39–55.
- [20] J. Xu, M. Lynch, J. L. Huff, C. Mosher, S. Vengasandra, G. Ding, and E. Henderson, “Microfabricated quill-type surface patterning tools for the creation of biological micro/nano arrays,” *Biomed. Microdevices*, vol. 6, no. 2, 2004, pp. 117–123.
- [21] E. H. Synge, “A suggested method for extending the microscopic resolution into the ultramicroscopic region,” *The London, Edinburgh, and Dublin Philosophical Magazine and J. Sci.*, vol. 6, 1928, pp. 356.
- [22] A. L. Lereu, A. Passian, and P. Dumas, “Near field optical microscopy: A brief review,” *International Journal of Nanotechnology*, vol. 9, no. 3–7, 2012, pp. 488–501.
- [23] E. Betzig, P. L. Finn, and J. S. Weiner, “Combined shear force and near-field scanning optical microscopy,” *Appl. Phys. Lett.*, vol. 60, 1992, p. 2484.
- [24] K. Karrai and R. D. Grober, “Piezoelectric tip-sample distance control for near field optical microscopes,” *Applied Physics Letters*, vol. 66, no. 14, 1995, pp. 1842–1844.
- [25] J. M. Vigoureux, C. Girard, and D. Courjon, “General principles of scanning tunneling optical microscopy,” *Opt. Lett.*, vol. 14, no. 19, 1989, pp. 1039–41.
- [26] U. C. Fischer and D. W. Pohl, “Observation of single-particle plasmons by near-field optical microscopy,” *Phys. Rev. Lett.*, vol. 62, no. 4, 1989, pp. 458–461.

- [27] P. Bazylewski, S. Ezugwu, and G. Fanchini, “A review of three-dimensional scanning near-field optical microscopy (3D-SNOM) and its applications in nanoscale light management,” *Appl. Sci.*, vol. 7, no. 10, 2017, p. 973.
- [28] J. M. Gerton, L. A. Wade, G. A. Lessard, Z. Ma, and S. R. Quake, “Tip-enhanced fluorescence microscopy at 10 nanometer resolution,” *Phys. Rev. Lett.*, vol. 93, no. 18, 2004, pp. 5–8.
- [29] B. Knoll and F. Keilmann, “Enhanced dielectric contrast in scattering-type scanning near-field optical microscopy,” *Opt. Commun.*, vol. 182, no. 4–6, 2000, pp. 321–328.
- [30] G. Wurtz, R. Bachelot, and P. Royer, “A reflection-mode apertureless scanning near-field optical microscope developed from a commercial scanning probe microscope,” *Rev. Sci. Instrum.*, vol. 69, no. 4, 1998, p. 1735.
- [31] J. Borrajo and L. Plata, “Validity of approximate equations for the calculation of the electron mean free path in terms of the size effect theory,” vol. 18, 1973, pp. 267–273.
- [32] L. Brus, “Quantum crystallites and nonlinear optics,” *Appl. Phys. A Solids Surfaces*, vol. 53, no. 6, 1991, pp. 465–474.
- [33] A. Bek, “Apertureless SNOM: A new tool for nano-optics,” vol. 3073, 2004, p. 110.
- [34] C. Genet and T. W. Ebbesen, “Light in tiny holes,” *Nature*, vol. 445, no. 7123, 2007, pp. 39–46.
- [35] B. Knoll and F. Keilmann, “Near-field probing of vibrational absorption for chemical microscopy,” *Nature*, vol. 399, no. 6732, 1999, pp. 134–137.
- [36] D. Haefliger, J. M. Plitzko, and R. Hillenbrand, “Contrast and scattering efficiency of scattering-type near-field optical probes,” *Appl. Phys. Lett.*, vol. 85, no. 19, 2004, pp. 4466–4468.
- [37] J. L. Bohn, D. J. Nesbitt, and A. Gallagher, “Field enhancement in apertureless near-field scanning optical microscopy,” *J. Opt. Soc. Am. A. Opt. Image Sci. Vis.*, vol. 18, no. 12, 2001, pp. 2998–3006.
- [38] B. Nicolas and M. B. Raschke, “Optical antenna properties of scanning probe tips: Plasmonic light scattering, tip-sample coupling, and near-field enhancement,” *The Journal of Physical Chemistry C*, vol. 112, no. 10, 2008, pp. 3766–3773.
- [39] N. Group, “Near-field microscopy by elastic light scattering from a tip,” *Philos. Trans. R. Soc. A Math. Phys. Eng. Sci.*, vol. 362, no. 1817, 2004, pp. 787–805.
- [40] J. D. Jackson, *Classical Electrodynamics*. New York, NY: Wiley, 1998.

- [41] N. Calander and M. Willander, “Theory of surface-plasmon resonance optical-field enhancement at prolate spheroids,” *J. Appl. Phys.*, vol. 92, no. 9, 2002, pp. 4878–4884.
- [42] J. Jersch, F. Demming, L. J. Hildenhagen, and K. Dickmann, “Field enhancement of optical radiation in the nearfield of scanning probe microscope tips,” vol. 34, 1998, pp. 29–34.
- [43] Ermushev, B. V. Mchedlishvili, and V. A. Oleynikov, “Surface enhancement of local optical fields and the lightning-rod effect,” *Quantum electron.*, vol. 23, no. 5, 1993, pp. 435–440.
- [44] A. Wokaun, “Surface enhancement of optical fields mechanism and applications,” *Mol. Phys.*, vol. 56, no. 1, 1985, pp. 1–33.
- [45] N. Ocelic, *Quantitative Near-Field*. Technische Universitat Munchen, 2007.
- [46] P. M. Krenz, R. L. Olmon, B. A. Lail, M. B. Raschke, and G. D. Boreman, “Near-field measurement of infrared coplanar strip transmission line attenuation and propagation constants,” *Opt. Express*, vol. 18, no. 21, 2010, pp. 21678–21686.
- [47] A. Cvitkovic, N. Ocelic, and R. Hillenbrand, “Analytical model for quantitative prediction of material contrasts in scattering-type near-field optical microscopy,” *Opt. Express*, vol. 15, no. 14, 2007, pp. 8550–65.
- [48] J. Stadler, C. Stanciu, C. Stupperich, and A. J. Meixner, “Tighter focusing with a parabolic mirror,” *Opt. Lett.*, vol. 33, no. 7, 2008, pp. 681–3.
- [49] E. Yoxall, “Applications of scattering-type scanning near-field optical microscopy in the infrared,” 2013.
- [50] B. Hecht and L. Novotny, *Principles of Nano-Optics*. New York: Cambridge University Press, 2006.
- [51] R. L. Olmon, M. Rang, P. M. Krenz, B. A. Lail, L. V. Saraf, G. D. Boreman, and M. B. Raschke, “Determination of electric-field, magnetic-field, and electric-current distributions of infrared optical antennas: A near-field optical vector network analyzer,” *Phys. Rev. Lett.*, vol. 105, no. 16, 2010, pp. 1–4.
- [52] J. M. Hoffmann, B. Hauer, and T. Taubner, “Antenna-enhanced infrared near-field nanospectroscopy of a polymer,” *Appl. Phys. Lett.*, vol. 101, no. 19, 2012.
- [53] A. C. Jones, R. L. Olmon, S. E. Skrabalak, B. J. Wiley, Y. N. Xia, and M. B. Raschke, “Mid-IR plasmonics: Near-field imaging of coherent plasmon modes of silver nanowires,” *Nano Lett.*, vol. 9, 2009, pp. 2553–2558.

- [54] M. Schnell, A. García-Etxarri, A. J. Huber, K. Crozier, J. Aizpurua, and R. Hillenbrand, “Controlling the near-field oscillations of loaded plasmonic nanoantennas,” *Nat. Photonics*, vol. 3, no. 5, 2009, pp. 287–291.
- [55] P. G. Gucciardi, G. Bachelier, S. J. Stranick, and M. Allegrini, “Background-free apertureless near-field optical imaging”, *Applied Scanning Probe Methods VIII*, 2008, pp. 1–29.
- [56] R. Hillenbrand, B. Knoll, and F. Keilmann, “Pure optical contrast in scattering-type scanning near-field microscopy,” vol. 202, pp. 77–83, 2001.
- [57] N. Ocelic, A. Huber, and R. Hillenbrand, “Pseudoheterodyne detection for background-free near-field spectroscopy,” *Appl. Phys. Lett.*, vol. 89, no. 1.
- [58] F. Physik, “Scattering scanning near-field optical microscopy on anisotropic dielectrics,” 2007.
- [59] SRS, “About Lock-In Amplifiers,” *Appl. Note*, no. 408, 2011, pp. 1–9.
- [60] S. Flyckt and C. Marmonier, “Photomultiplier tubes: Principles and applications,” *Photonis, Brive, Fr.*, 2002, pp. 265–304.
- [61] T. T. Tsong, *Atom-Probe Field Ion Microscopy*. Cambridge University Press, 1990.
- [62] M. K. Miller, A. Cerezo, M. G. Hetherington, and G. D. W. Smith, *Atom Probe Field Ion Microscopy*. Oxford University Press, 1996.
- [63] J. P. Ibe, P. P. Bey, S. L. Brandow, R. A. Brizzolara, N. A. Burnham, D. P. DiLella, K. P. Lee, C. R. K. Marrian, and R. J. Colton, “On the electrochemical etching of tips for scanning tunneling microscopy,” *J. Vac. Sci. Technol. A Vacuum, Surfaces, Film.*, vol. 8, no. 4, 1990, pp. 3570–3575.
- [64] D. Schrecongost, “Design of scattering scanning near-field optical microscope,” 2015.
- [65] H. Schweiger, P. Raybaud, G. Kresse, and H. Toulhoat, “Shape and Edge Sites Modifications of MoS₂ Catalytic Nanoparticles Induced by Working Conditions: A Theoretical Study,” *J. Catal.*, vol. 207, no. 1, 2002, pp. 76–87.
- [66] M. Sun, J. Adjaye, and A. E. Nelson, “Theoretical investigations of the structures and properties of molybdenum-based sulfide catalysts,” *Appl. Catal. A Gen.*, vol. 263, no. 2, 2004, pp. 131–143.
- [67] M. Fontana, T. Deppe, A. K. Boyd, M. Rinzan, A. Y. Liu, M. Paranjape, and P. Barbara, “Electron-hole transport and photovoltaic effect in gated MoS₂ Schottky junctions,” *Sci. Rep.*, vol. 3, no. 1, 2013, p. 1634.

- [68] W. Zhou, Z. Yin, Y. Du, X. Huang, Z. Zeng, Z. Fan, H. Liu, J. Wang, and H. Zhang, "Synthesis of few-layer MoS₂ nanosheet-coated TiO₂ nanobelt heterostructures for enhanced photocatalytic activities," *Small*, vol. 9, no. 1, 2013, pp. 140–147.
- [69] L. Yang, S. Wang, J. Mao, J. Deng, Q. Gao, Y. Tang, and O. G. Schmidt, "Hierarchical MoS₂/polyaniline nanowires with excellent electrochemical performance for lithium-ion batteries," *Adv. Mater.*, vol. 25, no. 8, 2013, pp. 1180–1184.
- [70] M. H. Cho, J. Ju, S. J. Kim, and H. Jang, "Tribological properties of solid lubricants (graphite, Sb₂S₃, MoS₂) for automotive brake friction materials," *Wear*, vol. 260, no. 7–8, 2006, pp. 855–860.
- [71] A. Splendiani, L. Sun, Y. Zhang, T. Li, J. Kim, C. Y. Chim, G. Galli, and F. Wang, "Emerging photoluminescence in monolayer MoS₂," *Nano Lett.*, vol. 10, no. 4, 2010, pp. 1271–1275.
- [72] K. F. Mak, C. Lee, J. Hone, J. Shan, and T. F. Heinz, "Atomically thin MoS₂: A new direct-gap semiconductor," *Phys. Rev. Lett.*, vol. 105, no. 13, 2010, pp. 2–5.
- [73] S. Balci, "Semiconductor nanowires: Towards enhanced terahertz sources," 2017.